Title
Magnetosome biogenesis in Magnetospirillum magneticum AMB-1

Author
Cornejo-Warner, Elias Jose

Publication Date
2016

Peer reviewed|Thesis/dissertation

Magnetosome biogenesis in *Magnetospirillum magneticum* AMB-1

By

Elias Jose Cornejo-Warner

A dissertation submitted in partial satisfaction of the

requirements for the degree of

Doctor of Philosophy

in

Microbiology

in the

Graduate Division

of the

University of California, Berkeley

Committee in charge:

Professor Arash Komeili, Chair
Professor Kathleen R. Ryan
Professor Michiko E. Taga
Professor Daniel A. Fletcher

Summer 2016

Abstract

Magnetosome biogenesis in *Magnetospirillum magneticum* AMB-1

by

Elias Jose Cornejo-Warner

Doctor of Philosophy in Microbiology

University of California, Berkeley

Professor Arash Komeili, Chair

The size, shape, and subcellular positioning of organelles in eukaryotes are optimized for their function and can dynamically respond to cellular demands (1, 2). Bacteria make a number of membrane-bound organelles but very little is understood about how the size and positioning of membrane-bound bacterial organelles influence their function (3, 4). This work explores the distinct structural features and dynamic properties that are linked to bacterial organelles. Specifically, this work uses *Magnetospirillum magneticum* AMB-1 as a model system to explores the formation and positioning of membrane-bound organelle, the magnetosome.

The first chapter of this dissertation, a published review article written in collaboration with a fellow Komeili lab member Nicole Abreu, introduces the topic of compartmentalization and subcellular organization in bacteria (4). Unlike eukaryotic cells, which share a specific set of organelles, bacteria possess a variety of morphologically and functionally distinct organelles that are not shared amongst all bacteria (3). Rather than describe all the bacterial organelles that have been discovered to date, chapter 1 provides vignettes of model organisms that exemplify different modes of membrane remodeling used to achieve compartmentalization. In addition, chapter 1 discusses the mechanisms that position a membrane-bound organelle and a protein-bound organelle from two model systems, magnetotactic bacteria and cyanobacteria.

The second chapter of this dissertation, a published primary research article, uncovers the dynamic nature of a membrane-bound bacterial organelle in the model magnetotactic bacterium. Magnetotactic bacteria make magnetic nanoparticles inside membrane-bound organelles called magnetosomes; however, it is unclear how the magnetosome membrane controls the biomineralization that occurs within this bacterial organelle. In collaboration with Grant Jensen's lab at Caltech, magnetosome formation was placed under inducible control in *Magnetospirillum magneticum* AMB-1 (AMB-1) and electron cryo-tomography was used to capture magnetosomes in their near-native state as they form *de novo*. An inducible system provided the key evidence that magnetosome membranes grow continuously unless they have not properly initiated biomineralization. Our finding that the size of a bacterial organelle impacts its biochemical function is a fundamental advance that impacts our perception of organelle formation in bacteria.

The third chapter of this dissertation (unpublished work) focuses on magnetosome organization and the positioning of newly formed magnetosomes in wildtype AMB-1. In a wildtype AMB-1,

the individual magnetosomes of a chain are at a different stages of formation, suggesting that magnetosomes are being made and added to the chain at different times (5). Indeed, maintaining a chain of magnetosomes over multiple cell generations would require the faithful segregation of the magnetosome chain by the mother cell, as well as the correct positioning of new magnetosomes in the daughter cells. To explore the spatial and temporal dynamics of magnetosome positioning, we developed a pulse-chase system to differentially label pre-existing versus newly formed magnetosomes. The preliminary data presented in chapter 3 provide evidence that this pulse-chase system can be used to identify sites of magnetosome biogenesis in relation to the pre-existing magnetosome chain. In addition, this system can be combined with time-lapse imaging to observe how the magnetosome chain is segregated and maintained over multiple cell divisions.

Table of Contents

CHAPTER 1

Compartmentalization and Organelle Formation in Bacteria

Elias Cornejo, Nicole Abreu and Arash Komeili

Department of Plant and Microbial Biology, University of California, Berkeley. USA

Abstract
A number of bacterial species rely on compartmentalization to gain specific functionalities that will provide them with a selective advantage. Here, we will highlight several of these modes of bacterial compartmentalization with an eye towards describing the mechanisms of their formation and their evolutionary origins. Spore formation in *Bacillus subtilis*, outer membrane biogenesis in Gram-negative bacteria and protein diffusion barriers of *Caulobacter crescentus* will be used to demonstrate the physical, chemical and compositional remodeling events that lead to compartmentalization. In addition, magnetosomes and carboxysomes will serve as models to examine the interplay between cytoskeletal systems and the subcellular positioning of organelles.

Introduction
The cell is crowded place and subcellular organization is vital to regulating its many metabolic processes (6). In eukaryotes, such organization is prominently achieved through the compartmentalization of biochemical reactions in various intracellular organelles. By limiting diffusion to a confined space, concentrations of enzymes and substrates can be optimized to promote specific enzymatic reactions. In turn, sequestration of activities within compartments protects the cell from toxic byproducts of such reactions. While historically considered to be simple cells with a low degree of subcellular differentiation, compartmentalization in the form of organelles is also a widespread phenomenon amongst bacterial cells (3). Unlike the eukaryotic endomembrane system, bacterial species are not equipped with a standard set of organelles. Instead, varying combinations of organelles provide unique capabilities to individual bacterial species. One notable class is the protein-bounded bacterial microcompartments, exemplified by the carbon-fixing carboxysomes of cyanobacteria (7). Lipid-bounded organelles, including the dazzling varieties of photosynthetic membranes found in heterotrophic bacteria and cyanobacteria, constitute another set of bacterial compartments (8–10). In addition to organelles, other modes of compartmentalization, such as the creation of spores and protein diffusion barriers to subdivide the cytoplasmic space, have also been described in bacterial cells (11, 12). Despite the impressive list of bacterial compartments and their cytological characterization, the molecular mechanisms that govern their formation, function and segregation are still a major question in bacterial cell biology. Here, we will focus on recent discoveries on the physical, chemical and compositional remodeling of membranes during compartmentalization as well as the mechanisms leading to the spacing and positioning of organelles within the cell. Those interested in acquiring a more in depth knowledge of this fascinating topic, are encouraged to read several recent review articles on the function, diversity and evolution of bacterial organelles (3, 13).

Membrane remodeling
A fundamental aspect of organelle formation in any organism is the remodeling of cellular membranes during the compartmentalization process. Remodeling can be physical in nature such as the bending, migration and fusion of lipid bilayers to produce and stabilize organelles. Chemical remodeling of lipids can also produce distinct compartments within the cell. Additionally, compositional remodeling of membrane domains, through protein targeting and/or exclusion, can subdivide a continuous structure into distinct compartments. These types of membrane remodeling have been described in numerous eukaryotic systems. In contrast, almost nothing is known about the methods and molecules used by bacteria to remodel their lipids into a

compartment. Here we highlight three cases where mechanisms and evolution of bacterial membrane remodeling events have been recently elucidated.

Physical remodeling: spore formation. Perhaps the most thoroughly studied example of membrane remodeling in bacteria is the engulfment of forespore during the sporulation process of *Bacillus subtilis*. When growth is challenged by harsh conditions, *B. subtilis* cells undergo a unique developmental program to form a highly durable and dormant endospore. During the early stages of sporulation, an asymmetric division event creates a larger "mother" cell that proceeds to engulf the smaller "forespore" cell to form an internal, double-membraned compartment (Figure 1a). A number of mechanisms have been implicated to drive the mother cell membrane around the forespore and have been recently reviewed (14). These include cell wall synthesis, cell wall degradation and specific protein interaction between SpoIIQ and SpoIIIAH that bridge across the mother and forespore membrane to prevent membrane retraction (Figure 1a)(14–17).

The final step of the engulfment process is the joining of the two ends of the migrating membranes to create a completely internalized endospore. Genetic analysis had implicated one protein, SpoIIIE, in membrane fission. However, *spoIIIE* null mutants also have defects in DNA translocation and septum morphology at earlier stages of sporulation raising the possibility that impaired membrane fission may be an indirect effect (18–20). By examining a set of mother cell genes that are expressed at the early stages of engulfment that when mutated, fail to release the forespore into the mother cell cytoplasm, Doan and colleagues recently identified fission protein B (FisB) as a direct catalyst of membrane fission in *B. subtilis* [16□□] (Figure 1a). Fluorescent protein fusions to FisB localize primarily to the edges of the migrating mother cell membrane that serve as the sites of membrane fission. Furthermore, purified FisB promotes membrane fusion *in vitro* via a specific interaction involving the extracellular domain of FisB and cardiolipin, an anionic phospholipid that is enriched in highly curved membranes including the forespore of *B. subtilis* (20–22). The authors propose that FisB may concentrate cardiolipin and create localized defects in the lipid bilayer that would favor the fission reaction. While these results highlight the importance of FisB in membrane fission, a small percentage of *fisB* mutants eventually complete engulfment, suggesting that alternative mechanisms may function at a slower rate to complete engulfment (20). A recent report identified core set of genes shared amongst sporulating bacteria, including three novel genes involved in endospore formation (23). This genomic signature may be a useful tool to identify additional mechanisms for membrane remodeling.

Chemical remodeling: Gram-negative outer membrane. Membrane remodeling is not limited to the physical movement and bending of lipid bilayers. Often, extensive modification of the chemical composition of cellular membranes is required for compartment formation and function. In bacteria, the construction of the Gram-negative outer membrane (OM) provides a model for understanding the mechanisms of chemical remodeling in biological membranes. As should be familiar to most students of biology, the Gram stain, developed by Hans Christian Gram in 1884, is a histological method for identifying and classifying bacterial species. Gram-positive bacteria have a single cell membrane that is surrounded by a thick, multi-layered cell wall. Gram-negative bacteria have two membranes separated by a thin cell wall (24) (Figure 1b). The OM displays a number of characteristics that define it as a bacterial compartment. It is an

asymmetric lipid bilayer with lipopolysaccharide (LPS), a glycolipid, on its outer leaflet and phospholipids on its inner leaflet. Beta-barrel proteins in the OM form pores that allow for non-specific exchange of small molecules with the extracellular environment while limiting diffusion of many cytoplasmically secreted proteins. Furthermore, the tight packing of LPS on the outer leaflet provides an impermeable barrier to small hydrophobic and hydrophilic molecules that can be harmful to the cell (24). The OM does not just function as barrier but also creates a chemically distinct periplasmic compartment where important processes, such as certain types of respiration, can occur.

While tremendous progress has been made in defining the chemical nature of the OM and uncovering the molecular mechanisms of its biogenesis (25, 26), the evolutionary origins of this structure have remained mysterious. A recent study has searched for the answer to this question by examining the curious mode by which some bacterial cells produce and germinate spores (27). Phylogenetically, most endospore forming bacteria fall under the *Bacilli* and *Clostridia* classes of the Gram-positive *Firmicutes* phylum (28). Interestingly, some members of the *Clostridia*, such as *Acetonema longum*, can form spores but are decidedly Gram-negative in their vegetative state, as they possess an inner membrane and an OM that contains LPS. Through high-resolution electron cryo-tomographic (ECT) imaging of *A. longum* and *B. subtilis* cells at different stages of sporulation and spore germination, Tocheva and colleagues were able to show that the inner membrane of the mother cell engulfs the forespore and forms the outer spore membrane (27, 29). During germination in *A. longum*, however, this membrane acquires the morphological and chemical signatures of an OM, including LPS (Figure 1b). Sequencing of the *A. longum* genome revealed the presence of homologs of genes known to encode for OM proteins in Gram-negative bacteria as well as those involved in sporulation in Gram-positives. Phylogenetic analysis showed that the OM proteins of *A. longum* do not cluster with those of other Gram-negatives whereas its sporulation proteins group with those of other Gram-positives. A parsimonious explanation for these results is that *A. longum* did not acquire the ability to produce an OM due to a recent horizontal gene transfer event, in which case its OM proteins would have been in tighter phylogenetic groups with homologs from Gram-negative organisms. Similarly, sporulation also seems to be an ancient characteristic of this organism. These findings lead to the tantalizing hypothesis that ancestors of Gram-positive and Gram-negative bacteria were able to link spore germination to construction of an OM. Subsequently, the majority of Gram-positives lost the ability to form an OM while the loss of sporulation genes gave rise to present-day Gram-negative organisms.

Compositional remodeling: protein diffusion barriers. Diffusion gradients are used by cells to control the timing and location of essential cellular processes (30). Protein diffusion barriers had only been described as a feature of eukaryotic cells until their recent discovery by Schlimpert and colleagues in the Gram-negative bacterium, *Caulobacter crescentus* (12, 3
1). At a specific point during its cell cycle, *C. crescentus* physically remodels its cell envelope to form a polar stalk that functions as a holdfast for attachment to surfaces. During phosphorus limiting growth periods the stalk undergoes a dramatic elongation leading to the hypothesis that it may have a role in phosphorus uptake from the environment. Even though the stalk is a protrusion of the cell envelope, Schlimpert and colleagues found that periplasmic proteins do not move between the stalk and the cell body. Furthermore, they found that the stalk itself was compartmentalized into several segments that restricted protein movement. Early electron

microscopic examination had found that curious cross band structures were spread throughout the *C. crescentus* stalk. Using a combination of genetic and biochemical approaches, the authors identified a protein complex consisting of four proteins (StpA, StpB, StpC and StpD) that localize to these conspicuous crossband structures. Deletions of the genes encoding the Stp factors result in a loss of cross band structures visualized by ECT and absence of compartmentalization within the stalk (Figure 2a). By preventing the accumulation of newly synthesized proteins into the stalk, these cross band structures essentially lead to a compositional remodeling of the compartment. One consequence of the loss of stalk compartmentalization is that proteins synthesized after stalk formation are no longer restricted to the cell body and are less concentrated in locales where their activity might be needed. This is especially of concern in phosphate starvation conditions in which the stalk elongates to the point that its surface area exceeds that of the cell body. In agreement with this model, the authors demonstrate that mutants missing the *stp* genes, take longer to accumulate proteins within their cell body and are outcompeted by wild-type cells in co-culturing experiments. Thus, in the case of the *C. crescentus* stalk, compositional remodeling partially acts to prevent the dilution of important cellular proteins (Figure 2b). Additionally, the authors hypothesize that the compositional remodeling of the stalk may also allow for localized activities that may be used to shuttle phosphate into the cell.

Organelle positioning

The subcellular positioning of compartments plays a key role in the function of many bacterial organelles. Recent studies have uncovered some of the molecular mechanisms that lead to the organization and positioning of two unique bacterial organelles, the magnetosome compartments of magnetotactic bacteria and the carboxysomes of cyanobacteria (32).

Compartmentalized through an invagination of the inner cell membrane, the magnetosome creates a controlled chemical environment optimal for formation and maturation of magnetite or greigite both of which are iron-based magnetic crystals. Magnetosome formation requires multiple steps utilizing genes that form membrane invaginations, localize proteins, nucleate crystals and align structures into a chain (5, 33–37). The end product of these processes is a well-aligned magnetosome chain (Figure 3a), which is thought to provide navigational capability towards preferred oxygen concentrations in a stratified water column, a process termed magnetoaerotaxis (38).

Subcellular organization of magnetosomes into a chain is dependent on MamK, a bacterial actin homolog that is present in all magnetotactic bacteria. High resolution imaging of *Magnetospirillum magneticum* AMB-1 by ECT revealed that organized chains of magnetosomes are flanked by filaments that disappear in a *mamK* deletion mutant (Figure 3a)(37). Much like other actin-like proteins, MamK forms filaments that are dynamic *in vivo* (39) and *in vitro* (40, 41) in a manner that is dependent on the ATPase activity of the protein. The dynamic behavior of MamK *in vivo* also relies on the redundant action of acidic proteins MamJ and LimJ (Figure 3a)(39). In their absence, MamK filaments are static as seen in a fluorescence recovery after photobleaching assay. In addition, the loss of *mamJ* and *limJ* results in multiple gaps within the magnetosome chain and a clustering of putative MamK filaments within these spaces. One interpretation of these results is that MamK dynamics may be acting to pull magnetosomes

together. Alternatively, the loss of MamJ and LimJ could change the localization of MamK in the cell leading to altered dynamics and an inability to form a coherent chain.

Despite the clear advances in understanding the behavior and properties of MamK as an actin-like protein, the specific mechanism by which it acts on the magnetosome chain remains unknown. The phenotypes of the *mamK* deletion strains are consistent with its action in either establishing or maintaining the magnetosome chain. Furthermore, in a related species, *Magnetospirillum gryphiswaldense* MSR-1, deletion of *mamK* results in ectopic chain localization and failure of partitioning the chain between daughter cells (42, 43). It has even been suggested that MamK acts to link physical forces on the magnetosome chain into changes in cell motility (44). Regardless of the specific mechanism of its action, MamK is clearly important for proper navigation in magnetic fields (45). A recent study using an agar plate magnetoaerotaxis assay found that *mamK* mutants had a significantly wider path around a magnetic field as compared to the wild type strain. In the environment, such a difference could translate into a longer travel period, and subsequently higher energy expenditure, for reaching a desired locale.

Similar to magnetosomes, the carboxysome organelles of cyanobacteria are also arranged linearly within a cell with a consistent spacing pattern. This arrangement relies on the action of the cytoskeletal protein, ParA, without which carboxysomes are unequally distributed amongst daughter cells (Figure 3b)(46). ParA filaments are also highly dynamic within the cell and undergo pole-to-pole oscillations that may be important in carboxysome positioning (Figure 3b). Given its crucial role in carbon fixation, the failure to acquire carboxysomes results in a significantly longer doubling time. ParA and its homologs belong to the Walker type family of ATPases and are often associated with segregation of plasmid or chromosomal DNA in diverse bacterial species. However, recent work has shown that a ParA homolog, PpfA, can also be used to segregate chemotaxis protein clusters during cell division in *Rhodobacter sphaeroides* (47). In this case, nonspecific interactions of PpfA with DNA as well as specific interactions with its chemotaxis protein cargo provide the means for separating the protein complexes (48). These findings leave open the possibility that in cyanobacteria, carboxysomes interact with chromosomes and that ParA is primarily directing the localization and segregation of DNA. However, deletion of *parA* does not affect the spacing of chromosomal DNA in cyanobacteria while disrupting the organization of carboxysomes (49). Thus, while DNA-ParA interactions may be important, specific interactions of this cytoskeletal protein with the carboxysome are likely needed for the proper positioning of this bacterial organelle.

Conclusion

The discovery of cytoskeletal elements, organelles and means of sophisticated spatio-temporal regulation in bacteria have transformed the simplistic views of this complex and metabolically diverse domain of life. The most fundamental roadblock in understanding compartmentalization comprehensively in bacteria is the scarcity of reliable model systems that can help to illuminate specific facets of the organelle formation process. As such, isolated examples of compartmentalization in genetically tractable organisms have carried the bulk of the weight in defining the mechanistic basis of membrane remodeling, protein localization and organelle segregation in bacteria. The diversity of these organelles and the specifications in their morphology and function makes it unlikely that a universal mechanism for compartmentalization exists amongst all bacteria. For instance, membrane remodeling in sporulation relies in part on

the use of peptidoglycan as a guide while no such cues will be available during magnetosome formation. Likewise, while magnetosomes and carboxysomes rely on cytoskeletal elements for their subcellular positioning, the proteins involved are not related hinting at distinct molecular activities in these two systems. Clearly, an expansion of available model organisms and a more thorough cataloging of bacterial organelles are needed to truly revolutionize this field. If successful, such endeavors will open new avenues of research in microbiology and uncover novel mechanisms of cell organization and compartmentalization.

Acknowledgements
Elias Cornejo is supported by award number R25GM090110 from the National Institute of General Medical Sciences and the National Science Foundation under Grant No. DGE 110640.The content is solely the responsibility of the authors and does not necessarily represent the official views of the National Institute of General Medical Sciences or the National Institutes of Health. Nicole Abreu is funded through the American Society for Microbiology's Robert D. Watkins Fellowship, UC Berkeley's Chancellors Fellowship and Mentored Research Awards.

Figures

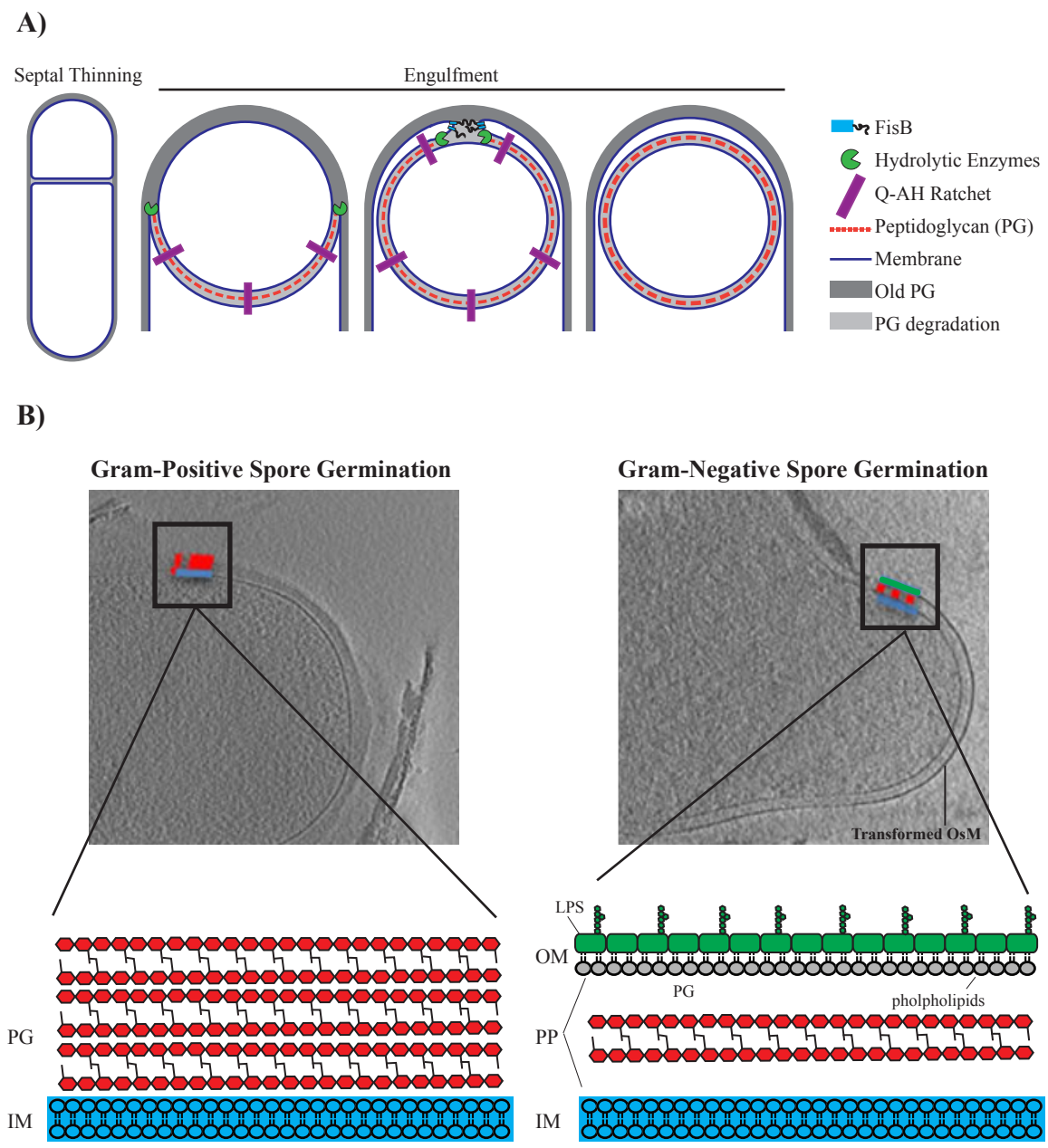

Figure 1A. Mechanisms of membrane remodeling during the different stages of engulfment. Engulfment initiates with degradation of septal peptidoglycan, commonly referred to as septal thinning. Peptidoglycan synthesis, peptidoglycan degradation and a specific "ratchet-like" mechanism that is mediated by proteins SpoIIQ and SpoIIIAH (Q-AH) are all factors that have been shown to be important for driving the mother cell membrane around the forespore. To be released into the mother cell, migrating membranes meet at the cell pole and undergo a fission event that is mediated by FisB. Note that the outer spore membrane (OsM) is derived from the cytoplasmic membrane of the mother cell.

Figure 1B. Spore germination of Gram-positive *Bacillus subtilis* (left) as compared to Gram-negative *Acetonema longum* (right). Upon germination, Gram-positive *Bacillus subtilis* (left) sheds its OsM whereas Gram-negative *Acetonema longum* (right) retains its OsM. Furthermore, *A. longum* transforms its OsM into a canonical Gram-negative outer membrane (OM). Cell envelope of Gram-negative vs. Gram-positive bacteria are very different. Gram-positive bacteria have a thick cell wall that is made up of multiple layers of peptidoglycan (PG) that surrounds an inner membrane (IM). On the other hand, Gram-negative bacteria maintain a thin layer of cell wall in-between two membranes. The OM of Gram-negative bacteria is compositionally different from the IM and creates a compartment, the periplasm (PP), that chemically distinct from the cytoplasm. The OM is an asymmetric bilayer with lipopolysaccharide (LPS) distributed in the outer leaflet and phospholipids distributed in the inner leaflet. [Tocheva et al., *Mol Micro*, 2013].

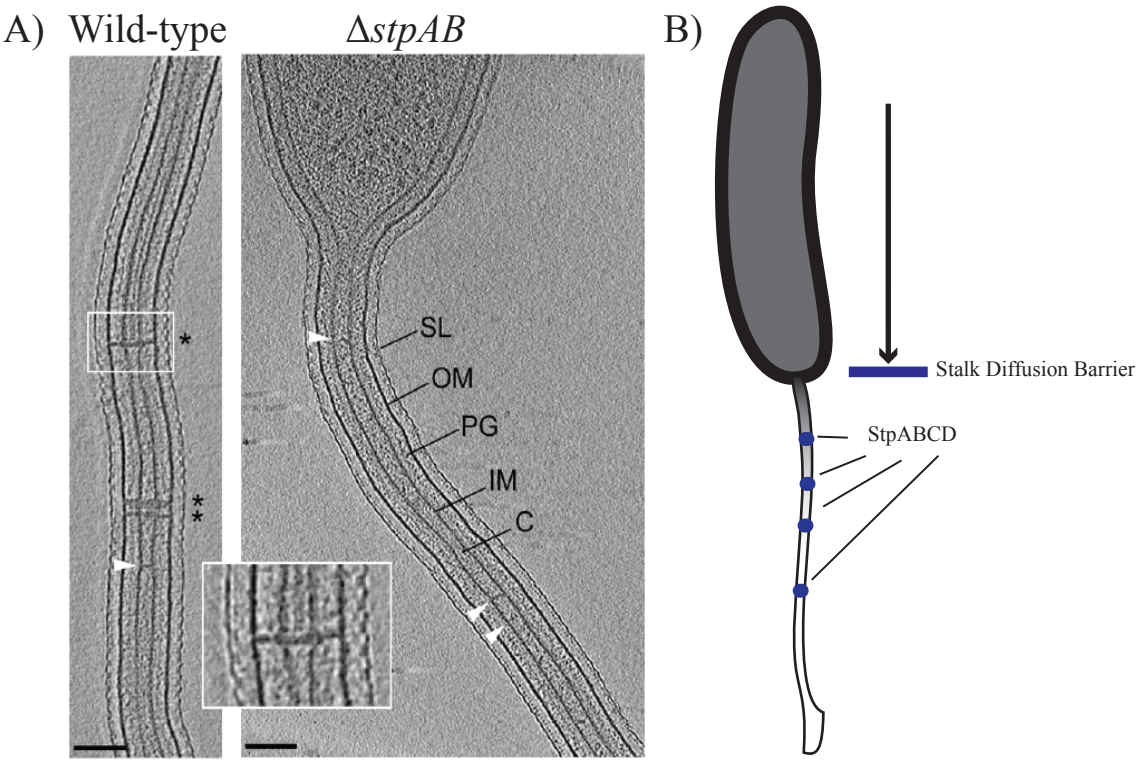

Figure 2. Diffusion barriers in *Caulobacter crescentus* stalk. A) Electron cryotomography images of wild-type *Caulobacter crescentus* cells containing stalk diffusion barriers (* and inset). Δ*stpAB* cells lack these structures. White arrows indicate unidentified structures that span the interior of the stalk (SL= S layer, OM= outer membrane, PG= peptidoglycan, IM= inner membrane, C= cytoplasm). Scale bar 100 nm. Reprinted from [Schlimpert et al., *Cell*, 2011] with permission from Elsevier. B) Stalk diffusion barriers: Comprising a protein complex of StpA, StpB, StpC and StpD (blue circles), diffusion barriers limit soluble and membrane protein diffusion into the stalk of *C. crescentus*.

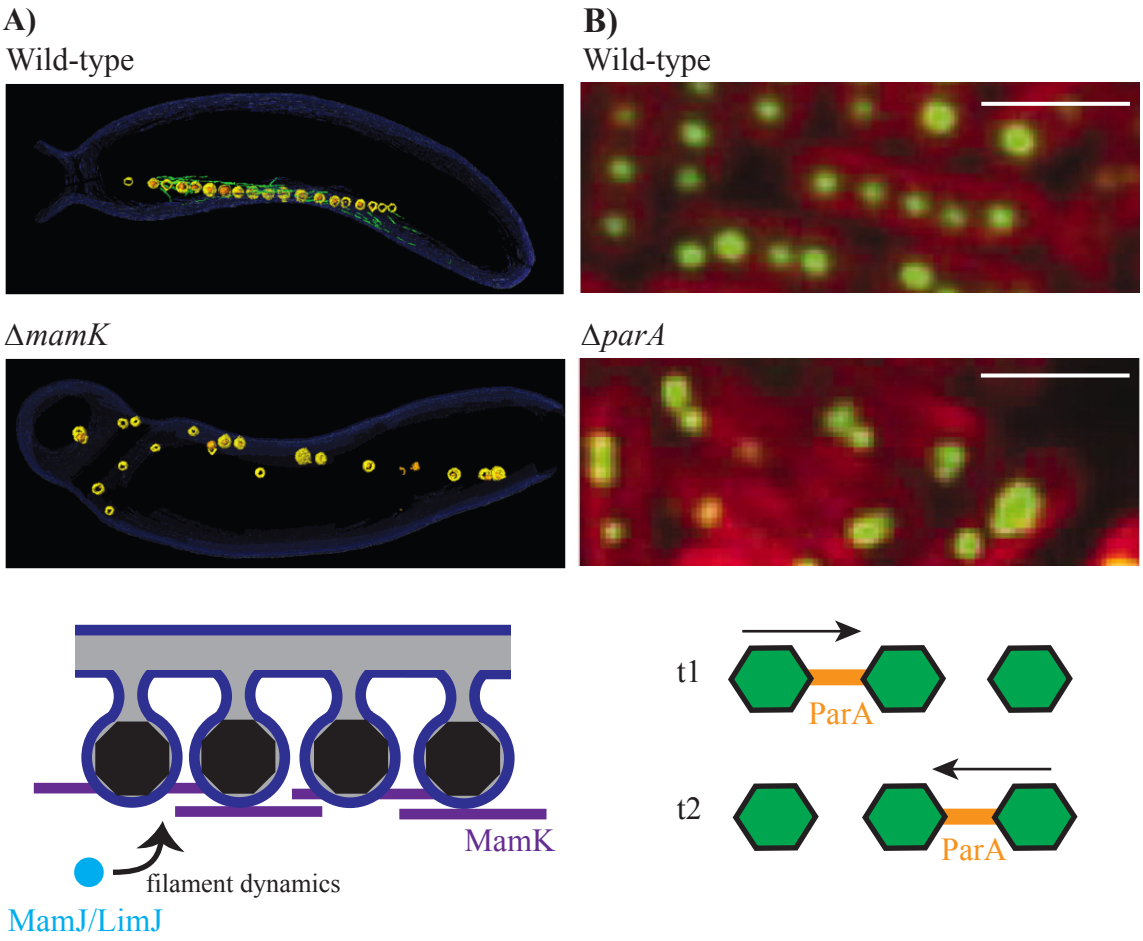

Figure 3. Organization of bacterial organelles by cytoskeletal filaments. A) The bacterial actin protein MamK is responsible for alignment of magnetosomes into a chain in Magentotactic Bacteria. Reconstructed electron cryotomography images of wild-type *Magnetospirillum magneticum* AMB-1 with an aligned magnetosome chain (top panel) and Δ*mamK* cells with disorganized magnetosomes (middle panel). The magnetosome (yellow) chain contains iron-based crystals (orange) and is flanked by filamentous structures (green) that disappear in the Δ*mamK* mutant. MamK dynamic filament behavior is influenced by the presence of MamJ and LimJ (bottome panel). The precise mechanisms that govern this process remain elusive. From [Komeili et al. Sceince, 2006]. Reprinted with permission from AAAS. B) Alignment and segregation of carboxysomes in cyanobacteria is dependent on ParA, another bacterial cytoskeletal protein. Carboxysomes are evenly distributed throughout the cell in wild-type *Synechococcus elongatus* PCC 7942 (top panel), but not in a mutant lacking *parA* (middle panel). Rubisco protein (RbcL) fused to YFP indicates the localization of carboxysomes (green) and thylakoid membrane fluorescence is shown in red. ParA oscillates from pole to pole and is found distributed in between carboxysomes (bottom panel). T1 and T2 represent time points that that are roughly 30 minutes apart. From [Savage et al., *Science*, 2010]. Reprinted with permission from AAAS. Scale bar 2 μm.

CHAPTER 2

Dynamic remodeling of the magnetosome membrane is triggered by the initiation of biomineralization

Elias Cornejo[a], Poorna Subramanian[b], Zhuo Li[b], Grant Jensen[b], Arash Komeili[a]

Department of Plant and Microbial Biology, University of California Berkeley, Berkeley, California, USA[a]; Department of Biology, California Institute of Technology, Pasadena, California, USA[b]

ABSTRACT

Magnetotactic bacteria produce chains of membrane-bound organelles that direct the biomineralization of magnetic nanoparticles (50). These magnetosome compartments are a model for studying the biogenesis and subcellular organization of bacterial organelles. Previous studies have suggested that discrete gene products build and assemble magnetosomes in a step-wise fashion (33). Here, using an inducible system, we show that the stages of magnetosome formation are highly dynamic and interconnected. During *de novo* formation, magnetosomes first organize into discontinuous chain fragments that are subsequently connected by the bacterial actin-like protein MamK. We also find that magnetosome membranes are not uniform in size and can grow in a biomineralization-dependent manner. In the absence of biomineralization, magnetosome membranes stall at a diameter of ~50 nm. Those that have initiated biomineralization then expand to significantly larger sizes and accommodate mature magnetic particles. We speculate that such a biomineralization-dependent checkpoint for membrane growth establishes the appropriate conditions within the magnetosome to ensure successful nucleation and growth of magnetic particles.

INTRODUCTION

Organelles are dynamic - their structure, composition, subcellular localization, and internal biochemical environment can change in response to cellular demands (1, 51–53). Bacteria possess a number of specialized protein-bound and membrane-bound compartments that can be vital for their survival in nature (3, 7). Similar to eukaryotes, some bacterial organelles are dynamic, undergo structural and compositional remodeling and require proper subcellular organization for faithful segregation amongst daughter cells (42, 46, 54–58). However, the molecular mechanisms of membrane remodeling to achieve the distinct morphologies, regulate the size, and segregate organelles in bacteria are not well understood.

Magnetotactic bacteria (MTB) produce membrane-bound compartments called magnetosomes that direct the formation of magnetic nanoparticles (50). Individual magnetosomes are organized into one or more chains that allow the cell to orient and navigate along geomagnetic fields (32, 59, 60). A series of previous biochemical, genetic and comparative genomic studies have identified a number of factors required for the formation and activity of magnetosomes (33–35, 37, 61–65). These analyses have led to a step-wise model for the assembly and function of magnetosomes in which membrane biogenesis, chain formation and biomineralization constitute distinct and separable stages (33, 34). Since this view is generated from static snapshots of mutant phenotypes, the spatiotemporal dynamics that might link the sequential stages of compartmentalization and biomineralization remain unexplored. For instance, it is unclear if the magnetosome membrane forms from a single-step deformation of the inner cell membrane or if it can dynamically expand throughout its development. There are also controversies regarding the molecular and physical mechanisms that create a chain of magnetosomes. Some studies have implicated magnetic interactions in magnetosome chain organization while others have not (33, 34, 66–68). Finally, it is unclear if the biochemical activity of the organelle in producing a magnetic biomineral influences its cell biological characteristics.

To address these outstanding issues, we designed a system to have inducible control over magnetosome membrane formation in *Magnetospirillum magneticum* AMB-1 (AMB-1). We show that magnetosomes formed in the absence of a pre-existing chain initially have a

discontinuous, but long-range alignment. The discontinuities in the chain are eventually corrected in a manner that is dependent on the bacterial actin-like protein, MamK. Surprisingly, we also find that individual magnetosome membranes show a dynamic two-step growth pattern. In the first step, a nascent magnetosome membrane is remodeled from the inner cell membrane, but does not grow beyond ~50 nm. A magnetosome membrane can continue to the second step of growth if, and only if, it has initiated biomineralization. We speculate that such a biomineralization checkpoint creates the proper environment for the formation of mature magnetite particles.

MATERIALS & METHODS

Bacterial Growth and Induction Conditions

Stock cultures were created from picking single colonies into 1.5 mL of defined minimal media (MG medium) supplemented with 1/100 volume of Wolfe's vitamin solution and 1/100 volume of 3 mM ferric chloride 9 mM malate as previously described (67). Cultures were incubated at 30° C for 48 hours, after which they are moved to room temperature. Stock cultures are good for 1-2 weeks at room temperature. Solid media plates contained 7 g agar per liter medium. Antibiotics were used at the following concentrations: kanamycin at 15 μg mL^{-1} in solid media and at 7 μg mL^{-1} in liquid cultures for strains where kanamycin resistant cassette was integrated into the chromosome.

For anaerobic growth, sealed Balch tubes containing 7 mL of MG media and 23 mL headspace were flushed briefly with N_2 gas after autoclaving and for 10 min. Once cooled, 1 of iron and vitamin mixture, diluted 1:10 each in MG, were added with a syringe. Lastly, 1 mL of inoculum cells was added from a stock culture that was diluted 1:10. Final concentration of iron, vitamins, and cells is 1:100.

Cells were induced with 1 mM theophylline and 1 mM IPTG. 20mM theophylline and 40 mM IPTG inducer stocks were prepared by dissolving the appropriate amount of solid inducer into MG media and sterilized by syringe filtration through a 0.2 μm sterile syringe filter.

Cmag time course and growth curve

Cultures were inoculated from 1:100 dilutions of stock culture into sealed Balch tubes as described above. Cultures were incubated at 30°C for approximately 16 -20 hours until the optical density of the cultures reached OD_{400} of .100-.150. Cultures were then passaged into fresh 10 mL sealed Balch tubes in triplicate and incubated at 30°C for an additional 16-20 hours until they reached an OD_{400} of .06. To induce, 750 μL of cell culture was removed and replaced with either 500 μL of 20mM theophylline and 250 μL of 40mM IPTG for induced group or with 750 μL of MG media for the uninduced group.

Fluorescence microscopy of induction time course

In order image cells during the induction time course by both FM and ECT, the culture volume was scaled up to from 10 mL to 100 mL in order to be able to allow for repeated sampling of the cell culture. To inoculate, 100 mL sealed-capped Balch bottles containing 90 mL of MG media were autoclaved then immediately flushed with N_2 gas for 10 minutes. 1 mL of 3mM ferric malate and 1 mL of 100X Wolfe's vitamins were added after bottles had been cooled to room temperature. The bottles were then inoculated 1:100 from a stock cell culture and incubated at 30°C approximately 16 -20 hours until the optical density of the culture reached

OD_{400} of .100. To induce, 5 mL of 20 mM theophylline and 2.5 mL 40 mM IPTG were added. In order to avoid over pressurizing the sealed capped bottles, an additional syringe needle was inserted into the rubber stopper while injecting contents to allow pressure to vent.

To sample, 1 mL of N_2 gas was injected into the bottle and 1 mL of cell culture was removed using the same syringe. The 1 mL cell culture sample was centrifuged at 14000 rpm for 3 minutes, then 750 µL of supernatant was removed and the remaining 250 µL was centrifuged at 14000 rpm again to obtain a cell pellet. The media was removed with a pipette and the cell pellet was resuspended in 50 µL of MG media.

Imaging by Fluorescence Microscopy, Transmission Electron Microscopy and Localization Pattern Quantification

Cells were induced in 100 mL sealed Balch cultures and sampled as described above. To image, 7 µL of resuspended cell pellet sample (sample collection described above) was spotted on agarose pad containing MG and 1% agarose, allowed to sit on bench top for 3 minutes before placing on coverslip. Coverslip was then sealed with Valap to prevent desiccation of agarose pad. Fluorescence microscopy was performed on Nikon Eclipse 80i microscope. Images were acquired at 1000X magnification using a QImaging RETIGA 2000R Fast 1394 camera. GFP-MmsF localization patterns were quantified using ImageJ Cell Counter plug-in to score each cell in the field of view to one of the four distinct localization patterns: membrane, unaligned foci, aligned foci, solid line (69). The localization patterns for >300 cells were determined for each time point per experiment. For imaging whole cells by TEM, 7 uL of resuspended cell pellet sample absorbed on a 200-mesh Cu grid coated with Formvar film and imaged on a FEI Technai 12 TEM of transmission electron microscopy (TEM) equipped with a Gatan Bioscan (1k x 1k) CCD Camera Model 792 at an accelerating voltage of 120 kV.

Magnetosome membrane and crystal size quantification

Tomogram reconstructions were visualized using the IMOD Version 4.7 software form developed by the University of Colorado (70). Cells were positioned using the Slicer function to determine magnetosome alignment and orient individual magnetosomes to determine the maximum diameter for magnetosome membrane and crystal. Membrane size is reported as the average of three independent diameter measurements from the orientation where the boundaries of the magnetosome membrane is most visible and is the largest. Crysal size is reported as the long axis (length) of the crystal.

Electron Cryo Tomography (ECT)

For all strains, 1.5 ml of cells were centrifuged at 14000 g for 3 minutes to obtain a pellet, which was resuspended in 50 µL of MG media. 16 µL of resuspended cells were mixed with 4 µL of BSA-treated 10 nm colloidal gold fiducial markers (71, 72). 4 µL of this mix were applied to a glow discharged, X-thick carbon-coated, R2/2 copper Quantifoil grid (Quantifoil Micro Tools) in a Vitrobot (FEI Company, Hillsboro, OR). The vitrobot chamber was maintained at a temperature of 22°C and humidity of 80%. Excess liquid was blotted off the grid with a blot force of 3, blot time of 2.5 s and drain time of 1 s. The grid was then plunge-frozen in a liquid ethane-propane mixture (73) and imaged by ECT. Imaging was performed on an FEI Polara™ G2 (FEI Company, Hillsboro, OR) 300 kV field emission gun electron microscope equipped with a Gatan image filter (Gatan, Pleasanton, CA) and K2 Summit™ counting electron detector

camera (Gatan, Pleasanton, CA). Data was collected using the UCSFtomo software (74) with each tilt series ranging from -60° to 60° in 1° increments, an underfocus of 15 μm and a cumulative electron dose of ~120 e/A^2 or less for each individual tilt-series. The RAPTOR software package was used to calculate 3D reconstructions (75).

Plasmids, primers and strains

The design for all plasmids, primers and strains used in this study are described and listed in Supplemental Materials and Methods.

Plasmid and Strain Design

riboswitch-*mamL*

A number of ligand inducible riboswitches had been synthetically engineered with affinity for the small molecule, theophylline to inducibly control the expression of *mamK-gfp* (76). We cloned *mamL* (*amb0966*) into pAK550 in between EcoRI and SpeI restriction sites using primers 5EcoL and 3SpeL to generate was pAK892.

lacI-riboswitch *mamL*

The Gibson cloning method was used to clone *lacI* along with its native promoter upstream of the *tac* promoter into the XhoI site of pAK892 (77). *lacI* was amplified off of pAK312 using primers oAKD25 and oAKD28 to generate pAK893. The lac operator from the tac promoter had been removed in the engineering of the synthetic riboswitch constructs. In order to return the *lac* operator sequence, a unique SwaI restriction site was inserted between the *tac* promoter and the riboswitch using primers oAKC19 and oAKC20 by QuikChange™ amplification to generate pAK894 (Stratagene). Next, the entire *lacI* and *tac* promoter were amplified by PCR using primers oAKD25 and oAKC21. A tight binding *lac* operator sequence (GAATTGTGAGCGCTCACAATT) was synthesized on the on the 3' end of the reverse primer oAKC21 (78). The amplified insert was cloned in the HindIII and SwaI sites of pAK894 to generate pAK895.

Integrative inducible *mamQ-M2*

The inducing module (*lacI* and riboswitch) and *mamQ-M2* were cloned in several steps in the into the integrative plasmid pAK605, which integrates into the intergenic region between *amb0397* and *amb0398* outside of the magnetosome gene island (MAI). In the first step, the inducing module was amplified off of pAK895 using primers oAKD10 and oAKD13 and cloned between BamHI and SpeI sites on pAK605 to make pAK739. The *mms16* promoter was amplified off of pAK54 using primers oAKD62 and oAKD63 and cloned into the NotI restriction sites of pAK605 using by Gibson cloning method. The resulting plasmid, pAK741, has the inducing module and *mms16* promoter reading into each other in a tail-to-tail fashion. A version of *mamQ* (*amb0972*) that lacked its stop codon was amplified off of genomic DNA using primers 5SpeQ and oAKC51 and cloned into and SpeI and BamHI sites of pAK702 to construct pAK732. *mamQ-M2* was amplified off of pAK732 using primers oAKE07 and oAKE12 and cloned downstream of the riboswitch on pAK741 into the SpeI site by Gibson

cloning. The resulting pAK749 plasmid consists of *lacI* with its native promoter, *tac* promoter with a tight binding *lac* operator, a riboswitch, *mamQ-M2*, reading in the 5' to 3' direction and the *mms16* promoter downstream of *mamQ-M2* reading in the 3' to 5' direction.

Allelic replacement of *mmsF* and generation of inducible strains

A two-step recombination method was used to delete *mamK* in the LD9ΔQ strain (AK46) as previously described (67). The same two-step recombination method was used to replace *mmsF* (*amb0957*) with *gfp-mmsF*. Briefly, an approximately 1 kb region upstream and downstream of amb0957 were amplified off of genomic DNA using primers pairs (oAKF02, oAKF03) and (oAKF04, oAKF05) respectively. *Gfp-mmsF* was amplified off of pAK532 using primers oAKE69 and oAKE70. The three pieces were cloned into the SpeI restriction site of the pAK0 suicide plasmid using the Gibson cloning method to generate pAK897. pAK897 was conjugated into AMB-1 wildtype (AK30), LD9ΔQ (AK46) and LD9ΔQΔK (AK166) using E.coli WM3064 donor strain. Colonies that had successfully integrated the plasmid were selected on MG agar plates containing kanamycin (15 μg mL^{-1}). To select for colonies that had undergone a second recombination event to lose the integrated plasmid, a counter-selectable marker *sacB*, which is toxic in the presence of sucrose, was used. Colonies were passaged in 10 mL of growth media without kanamyacin and plated on MG plates containing 1% sucrose. The resulting sucrose resistant colonies were checked for the successful integration of *gfp-mmsF* at its native locus by colony PCR and complementation was verified by Cmag and fluorescence microscopy.

To generate inducible strains AK167 (Q_{Ind}) and AK203(Q_{Ind}ΔK), pAK748 was conjugated into AK168 and AK202 respectively. Integration of pAK748 into the intergenic region between *amb0397* and *amb0398* was selected for on MG plates with kanamyacin and verified by colony PCR for *mamQ-M2*. Counter selection for *sacB* was not carried out since the entire plasmid was integrated into the chromosome.

RESULTS

Magnetosome formation can be placed under inducible control.

In order to control magnetosome formation, we sought to complement a mutant strain incapable of producing magnetosomes with its missing gene in an inducible fashion. In AMB-1, four genes appear to be necessary, but not sufficient, to make the magnetosome membrane compartment: *mamI, mamL, mamQ,* and *mamB* (33). We screened N-terminal and C-terminal M2-tagged versions of each of these required genes and found that M2-tagged *mamQ* could restore the magnetic phenotype of the *ΔmamQΔR9* genetic background (LD9ΔQ) that lacks both functional copies of *mamQ* (Fig. S1D). To ensure full repression of the inducible gene, *mamQ-M2* was placed under the control of a combination of a LacI-repressed promoter and a translationally repressed synthetic riboswitch (Fig. S1A) (76). Additionally, the copy number of the inducible construct was reduced by integration into a neutral site in the chromosome. In this context, the expression of *mamQ-M2* and magnetosome formation was successfully repressed in the LD9ΔQ strain (Fig. S1A). Western blotting using antibodies against the M2 tag shows that no detectable MamQ-M2 is produced in the absence of the inducers and that maximal induction occurs when both inducers, IPTG and theophylline, are introduced (Fig. S1B and S1C). In this configuration, the riboswitch appears to be a more potent inhibitor since it is required to repress

leaky transcription from *lacI* even when both constructs were integrated into the chromosome (Fig. S1C).

Magnetosome formation in the inducible strain (referred to as Q_{Ind} for simplicity) was assessed by monitoring chain formation and the development of a cellular magnetic response. The localization of a magnetosome protein, MmsF, fused to GFP (GFP-MmsF) was used to visualize the development of magnetosome chains during induction. MmsF is a 124 amino acid transmembrane protein of unknown function that has been shown to control the size and shape of magnetic particles in AMB-1 (37, 79). GFP-MmsF complements the small crystal phenotype of the *mmsF* deletion strain (37). Furthermore, GFP-MmsF localizes to the magnetosome chain in both wildtype and *ΔmmsF* strains and uniformly around the cytoplasmic membrane in strains that are incapable of making magnetosomes (37). We integrated *gfp-mmsF* into the chromosome of the Q_{Ind} strain by allelic replacement of the native copy of *mmsF*. In the uninduced state, GFP-MmsF localizes uniformly around the inner membrane in the Q_{Ind} strain. However, GFP-MmsF gradually acquires a linear localization pattern when Q_{Ind} is induced for 6 hours (Fig. 1A and 1B). The first change in the localization pattern is observed at 2 hours post-induction (hpi), where 44 ± 9% of the cell population has unaligned foci of GFP-MmsF and 18 ± 4% of the population has aligned foci (Fig. 1A and 1B). At 3 hpi, the percentage of cells with a linear localization pattern of GFP-MmsF, either aligned foci or solid lines, increases to 46 ± 13% (Fig. 1A and 1B). By 6 hpi, 86 ± 9% of the population displays a linear localization pattern of GFP-MmsF (Fig. 1A and 1B). In addition, we assessed if the induced magnetosomes were functional by measuring the coefficient of magnetism (Cmag) of the cell culture over time (Fig. 1C). This measurement relies on the differential light scattering properties of a culture as cells are aligned perpendicular or parallel relative to the light beam via an external magnetic field. Uninduced cultures were non-magnetic, but could be induced to have a weak magnetic response at 4 hpi, which drastically increased by 6 hpi (Fig. 1C). Consistent with these measurements, transmission electron microscopy confirmed the development of mature magnetosome chains during the time course experiment (Fig. S1E). Taken together, these results show that magnetosome formation can be placed under inducible control and that the developmental stages of chain formation and biomineralization can be followed over time.

The combination of GFP-MmsF imaging and Cmag measurements imply that magnetosome membranes are most likely formed early in the time course experiment prior to the development of magnetic biominerals. In order to visualize these early membrane dynamics at a high resolution, we performed electron cryotomography (ECT) on cells sampled throughout the induction time course. In previous work, wildtype-like assemblies of empty magnetosome membranes were absent from LD9ΔQ cells that were chemically fixed, sectioned and imaged with conventional transmission electron microscopy (33). However, in ECT imaging cellular membranes and subcellular structures are very well preserved in a near native state eliminating artifacts that arise from chemical fixing or sectioning (80, 81). In the LD9ΔQ strain we observe structures that have some magnetosome-like characteristics (Fig. S2). Similar to magnetosomes, these structures can be membrane-bound and in rare cases, even contain electron-dense particles reminiscent of early biomineralization. However, these structures are also distinct from magnetosomes since they occur mostly in isolation, lack fully formed magnetic crystals and are not flanked by filaments. Since it cannot be ruled out that these structures are magnetosomes, we imposed strict criteria to positively identify magnetosomes versus other membrane structures. Therefore, for the rest of the ECT work presented here, a feature was only included in the analysis if it was connected, or in close proximity, to the inner membrane and if it was adjacent

to other structures resembling magnetosomes. These criteria allowed us to distinguish magnetosomes that are being assembled into a chain from background cytoplasmic vesicles, misaligned magnetosomes and other inner membrane features that may also be present in the cell.

Despite the presence of isolated cytoplasmic membrane structures in the uninduced condition, we observed an increase in the number of magnetosomes within the cell at 1 hpi (Fig. 1D). In bacteria, subcellular organization is oftentimes achieved by directing proteins and processes to particular cellular locations, such as the cell pole or the midcell (82). However, we were not able to discern any distinct or dedicated sites of magnetosome biogenesis. Thus, in the context of the inducible system, the machinery required to form the magnetosome compartment may be distributed at multiple sites throughout the inner membrane.

Magnetosome chain organization: alignment pattern and chain continuity

In addition to investigating the morphology and spatial organization of early magnetosome formation events, we used the inducible system to define the pattern, dynamics and molecular requirements for chain formation over time. To better define the temporal properties and dynamics of chain formation during the induction, we determined the distance between adjacent magnetosomes to derive a quantitative measure of chain continuity. In wildtype cells, the average edge-to-edge distance between adjacent magnetosomes is 28.7 nanometers (nm) and only 5.4% of distances exceed 75 nm (Fig. S3). Based on our observations of magnetosome spacing in wildtype, an inter-magnetosome measurement was considered a gap if its edge-to-edge distance exceeded 75nm. When magnetosome formation was induced in the Q_{Ind} strain, clearly aligned but discontinuous chains of magnetosomes were observed at 3 hpi (Fig. 2A). The average distance between adjacent magnetosomes is 64.6 nm and 21.6% of distances constitute a gap (Fig. 2C). Over time, the number of gaps in Q_{Ind} decreases to essentially wildtype levels and only 5.1% of distances are gaps at 5 hpi (Fig. 2A and 2C). These findings show that in the absence of a pre-existing chain, clusters of magnetosomes are separated by a number of gaps but still maintain a long-range alignment across the cell. These discontinuities are then closed to form a magnetosome chain.

Previous studies have shown that in AMB-1, the loss of *mamK* results in a chain organization defect where gaps between adjacent magnetosomes occur within the chain (5). MamK forms dynamic filaments *in vivo* and *in vitro* in an ATP-dependent manner, but the exact role of MamK in chain organization is unclear (39, 40). In order to better understand the role of MamK in magnetosome chain formation, we deleted *mamK* in the inducible strain (creating $Q_{Ind}\Delta K$) and induced magnetosome formation to observe *de novo* chain assembly. Much like inducing magnetosome formation in the Q_{Ind} background, a clear chain of aligned magnetosomes with a number of gaps is visible at 3 hpi (Fig. 2B). These gaps account for 42.6% of the inter-magnetosome distances measured in the population (Fig. 2C). Unlike the induced Q_{Ind} strain, however, in which these gaps eventually disappear, the $Q_{Ind}\Delta K$ strain still retains large gaps in the magnetosome chain (Fig. 2B and 2D). Indeed, at 5 hpi 39.2% of the pairwise distances measured between adjacent magnetosomes are still gaps (Fig. 3C).

These results suggest that two distinct organizational principles govern magnetosome chain formation: magnetosome alignment and chain continuity. Alignment is a long-range mechanism to establish an axis for the magnetosome chain, whereas chain continuity is a short-range mechanism that closes the gaps between two adjacent magnetosomes. Alignment appears to occur first, in a manner that is independent of *mamK*. Once long-range alignment is established, the gaps between adjacent magnetosomes are closed in a manner that is dependent

on *mamK*. We speculate that MamK could act to fill the gaps either though guiding the direct synthesis of new magnetosomes within the gaps, recruiting existing but misaligned magnetosomes to the gaps or by physically pulling adjacent magnetosomes together to close the gaps. Real time microscopy techniques that independently track newly formed magnetosomes versus pre-existing magnetosomes could potentially distinguish between these different models and elucidate how MamK closes gaps to form a continuous magnetosome chain.

There are likely additional forces involved in the subcellular organization of magnetosomes that remain to be discovered. It has been proposed that the magnetic interactions between magnetosomes could facilitate chain formation, since inducing biomineralization in a closely related magnetotactic bacterium, *Magnetospirillum gryphiswaldense* MSR-1 (MSR-1), results in a rapid reorganization of magnetosomes into a chain (66). Since *de novo* chain formation occurs within five hours of the induction time course, when only 3% of the magnetosomes contain magnetic particles, it is clear that magnetic interactions between magnetosomes are not required to form a magnetosome chain in AMB-1 (Fig. 2A and 2B). Even though other candidate cytoskeletal proteins, such as FtsZ-like and MamK-like, exist in AMB-1, we did not find magnetosome-associated filaments in the absence of MamK or between distantly aligned magnetosomes in the Q_{Ind} strain by ECT (83–85). A long-range alignment factor or combination of factors therefore remains to be discovered.

Magnetosome membrane compartments are dynamic structures that can increase in size.

It is not known if the size of the membrane ultimately determines the size of the crystal or if the growth of the mineral can lead to a change in membrane size. One possibility is that one-step remodeling of the cytoplasmic membrane creates a magnetosome membrane compartment of a pre-determined size that provides the ultimate boundaries to control the size of the growing mineral. Alternatively, the magnetosome membrane could expand continuously in conjunction with a growing crystal. By examining the size of magnetosomes in the Q_{Ind} induction time-course experiment, we find that at 1 hpi, magnetosome membrane diameter has an approximately normal distribution with a mean of 29.4 ± 5.0 nm (Fig. 3A and Table S1). This distribution shifts to 38.5 ± 5.5 nm at 3 hpi and then again to 42.4 ± 5.2 nm at 5 hpi (Fig. 3A, Fig. S4A and Table S1). Based on two independent statistical analyses, Student t-test and Mann-Whitney U-test, there is a significant increase in both the mean and median of the membrane size distributions from 1 hpi to 3 hpi ($p < 1E-05$) and from 3 hpi to 5 hpi ($p < 0.05$) (Table S2) (86). A shift in the entire distribution at each time point suggests that the increase in size is not due to the one-step production of larger magnetosomes at later time points (Fig. 3A, Fig. S4A and Table S1). Instead, these results strongly argue that magnetosomes continually increase in size after the initial membrane invagination event.

The observations of magnetosome membrane growth in the inducible system prompted us to search for evidence of this dynamic behavior in wildtype cells. Indeed, when wildtype cells at steady state were imaged by ECT, a range of magnetosome membrane sizes from roughly 20 nm to 70 nm were observed (Fig. 3B). Curiously, magnetosomes that lacked electron dense nanoparticles did not exceed ~50 nm in diameter (Fig. 3B, Fig. S4A and Table S1). These smaller empty magnetosome membranes could represent defective compartments incapable of supporting biomineralization or they may hint at a link between magnetite formation and membrane growth. To distinguish between these possibilities, we compared membrane size distribution in wildtype cultures grown in iron-rich (+Fe) to those cultivated in iron-poor conditions (-Fe). In previous studies we have shown than in –Fe conditions nearly all

magnetosomes membranes are devoid of magnetite particles (Fig. 3C) (5, 67). These empty magnetosomes are functional for biomineralization since a shift to +Fe conditions results in rapid initiation of magnetite formation within them (35, 67). Interestingly, the diameter of -Fe magnetosomes (38.2 ± 4.7 nm) is significantly less than the diameter of +Fe magnetosomes (48.5 ± 11.7 nm) (Fig. 3C, Tables S1 and S2). In fact, in the –Fe cells no magnetosome membranes were larger than 55 nm whereas the +Fe cells had magnetosomes ranging in size from 21 nm to 79 nm (Fig 3C and Table S1). Taken together, these findings suggest that magnetosomes that have not initiated crystal formation are limited in size and that biomineralization is required for further membrane expansion.

Curiously, for the magnetosomes that have initiated biomineralization, a linear relationship exists between the size of the magnetosome membrane and the size of its resident crystal such that the largest magnetosome membranes contain the largest magnetite particles (Fig. 4A and 4B). Two potential models can be used to explain this observed relationship between magnetosome membrane size and biomineralization. First, it is possible that growth of the mineral physically distends the membrane and provides the force for its expansion beyond ~50 nm. Second, the initiation of biomineralization may be a regulatory cue that signals the expansion of the magnetosome membrane, thus providing a larger space for continued mineral growth. In order to explore if crystal growth physically expands the membrane, we measured the membrane diameter in the biomineralization mutant strain, *ΔmmsF*. Previous studies have shown *ΔmmsF* makes small crystals whose growth stalls at about 25 nm in length (37). If crystal growth physically expands the magnetosome membrane, then the *ΔmmsF* mutant should have a distribution of membrane diameters that is shifted to the smaller size range. However, in the *ΔmmsF* strain the magnetosome membranes can grow to full size independent of crystal size (Fig. 4C and 4D). In other words, the magnetosomes that harbor small crystals in *ΔmmsF* can grow as large as magnetosomes in wildtype that harbor mature crystals. The mean size distribution of magnetosome membranes of *ΔmmsF* (47.9 ± 8.6 nm) is similar to wildtype (45.8 ± 11.5 nm) despite its crystal maturation defect (Fig. 4E, Fig. S4A and Table S1). Additionally, similar to wildtype, the empty magnetosomes of *ΔmmsF* are significantly smaller in diameter than the magnetosomes that contain crystals (Fig. S4B). These results show that the physical forces of the growing crystal are not directly expanding the membrane. Instead, biomineralization triggers a release from a checkpoint that limits magnetosome membrane growth (Fig. 5). This commitment step for the second phase of membrane growth is downstream of crystal initiation but upstream of MmsF activity.

Discussion

Optimizing organelle size is often crucial for its cellular function (2). In eukaryotes, the nucleus and vacuole scale in proportion to cell size and defects in this scaling results in impaired fitness (2, 87). Likewise, organelles, such as mitochondria in yeast and photosynthetic membranes in bacteria, can dynamically change their size and morphology to adapt to changing environmental conditions (52, 54). Here, we provide evidence that magnetosomes, a bacterial organelle system, also have mechanisms in place to regulate their size and subcellular positioning in order to properly carry out their cellular function.

Previous studies had suggested that magnetic interaction between neighboring magnetosomes could play a role in organizing the chain (66, 68). These were disputed by findings that cells grown without iron and nonmagnetic mutants still contain intact chains of empty magnetosomes (33, 67). However, it could be argued that the preexisting chain in these

cases served as a landmark for the recruitment of empty magnetosomes to the chain. By using an inducible system in a mutant devoid of magnetosomes, we were able to show that chain assembly can be accomplished, *de novo*, without the aid of magnetic interactions. In addition, we identified two time-resolved stages to the chain assembly process. First, several clusters of magnetosomes, separated by large gaps, are aligned over a long range across the long cell axis. Next, with the help of MamK, these gaps are closed to form a full chain.

Much like what we observed here, previous ECT imaging of mutants had shown that in the absence of *mamK* the magnetosome chain loses its continuity and clusters of magnetosomes are separated by gaps (5, 43). This phenotype could arise as a result of a failure to establish the chain, to maintain it after its formation, or as has been suggested in MSR-1, to properly segregate it across multiple cell divisions (42). However, given the 4-6 hour doubling time of AMB-1, missegregation events occurring over many cell divisions cannot account for the chain formation defects observed in the absence of *mamK* in the induction experiment. By reconstructing the magnetosome chain *de novo* we rule out chain segregation as a main driver of the Δ*mamK* mutant phenotype. Instead, we propose two distinct stages of magnetosome chain formation, long rang alignment and chain continuity, and show that *mamK* is required for the latter.

Our most unexpected finding is that the magnetosome membrane grows in a manner that is regulated by a biomineralization-dependent checkpoint. In eukaryotes, a number of membrane remodeling mechanisms exist to achieve the distinct sizes and morphologies of organelles (88–90). Magnetosomes membranes do not appear to be remodeled to a fixed size, such as the cargo-specific size of endocytic vesicles generated through clathrin-mediated endocytosis (91). Instead, magnetosomes seem to undergo continuous membrane remodeling similar to the endoplasmic reticulum and mitochondria (92, 93). It is unclear if the membrane remodeling mechanisms identified in eukaryotes hold true for bacteria. However, we speculate that magnetosomes could grow by insertion or oligomerization of curvature-inducing proteins into the membrane, exchange of material between magnetosomes and the cytoplasmic membrane, or even protein/lipid delivery through fusion with cytoplasmic vesicles. It is also remarkable that throughout its growth the magnetosome membrane maintains the same overall morphology of a sphere connected to the inner cell membrane through a narrow invagination. This possibly implies the presence of a scaffold that maintains a uniform spherical architecture and perhaps a collar to stabilize the highly curved neck. In eukaryotes, Bin/amphiphysin/Rvs (BAR) domain containing proteins have been shown to bind and stabilize curved membranes due to their naturally curved domain architecture (89, 94). In AMB-1, *mamY* encodes a putative BAR domain whose deletion results in larger magnetosome membranes (67.9 nm) than wildtype (60.1 nm) (95). However, this modest change is size does not appear to impact membrane morphology or biomineralization and there are likely other factors that control and stabilize magnetosome membrane size and shape.

Finally, the coordination of membrane growth with the onset of biomineralization implies that the size of the organelle is crucial in the development of its final product. It is possible that restricting the volume of the magnetosome lumen provides an efficient means of reaching supersaturated iron levels in order to properly nucleate magnetite (96). Alternatively, as we have speculated previously, a biomineralization-driven checkpoint could result in smaller magnetite particles that are stalled in a superparamagnetic state and unable to commit the organism to a magnetotactic lifestyle (35). Changes in conditions favorable for magnetoaerotaxis would rapidly lead to membrane growth and development of large stable magnets. Our findings in this work have profound consequences for understanding the cell biology of magnetosome organelle

formation and the regulation of biomineral formation. Understanding size control and membrane remodeling as it pertains to making magnetic particles within magnetosomes may ultimately lead to a broader understanding of organelle development in other bacterial systems. Additionally, magnetite displays size-dependent changes in its magnetic properties (97). As such, the molecular understanding of membrane size determination will allow for more precise control over the design of synthetic magnetic particles for future industrial applications.

Figures

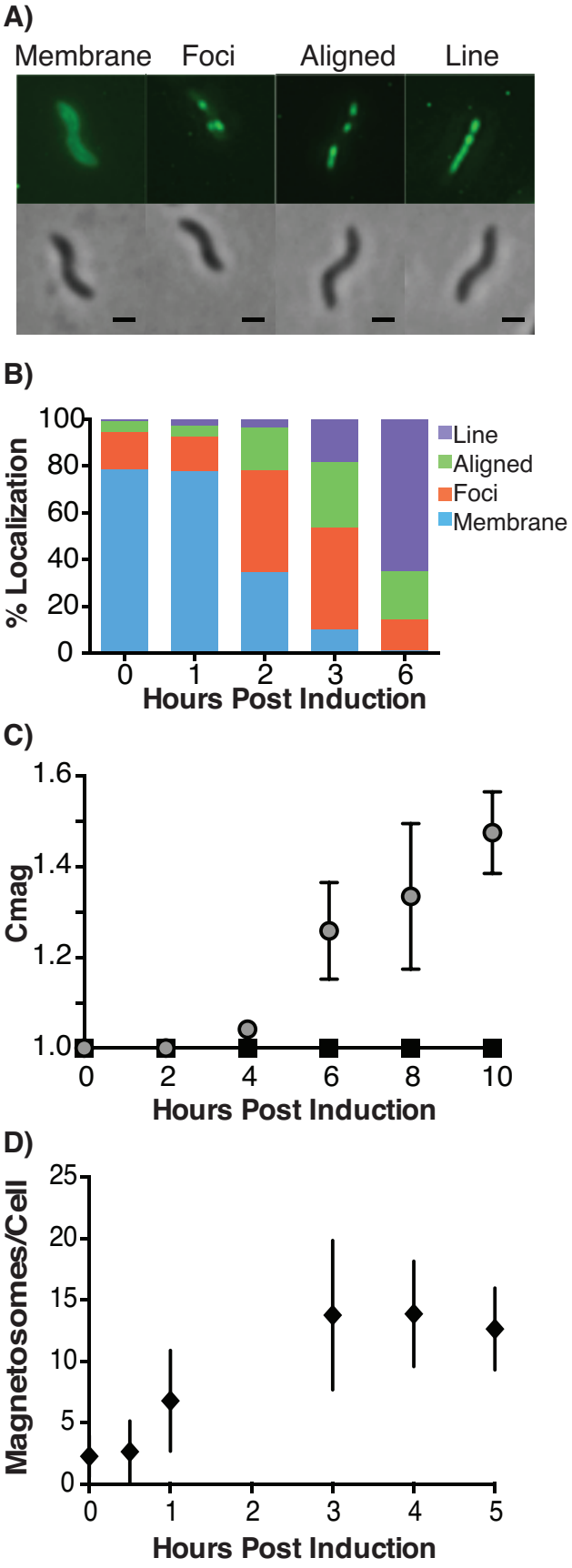

Figure 1: Magnetosome formation can be placed under genetically inducible control to follow de novo magnetosome formation and organization. (A) GFP-MmsF can be classified into 4 distinct localization patterns: membrane localized, unaligned foci, aligned foci and a solid line (scale bar = 500 nm). (B) Mean localization pattern of GFP-MmsF for three independent 6-hour induction timecourses. (C) Magnetite crystal formation is assessed by the degree of magnetic response (Cmag) of triplicate cell culture induced over a 10-hour timecourse. (D) Quantification of the mean number of magnetosomes per cell that could be visualized by electron crytomography (ECT) over a 5-hour time course. 7-10 tomograms of the induced cell population were reconstructed for each time point.

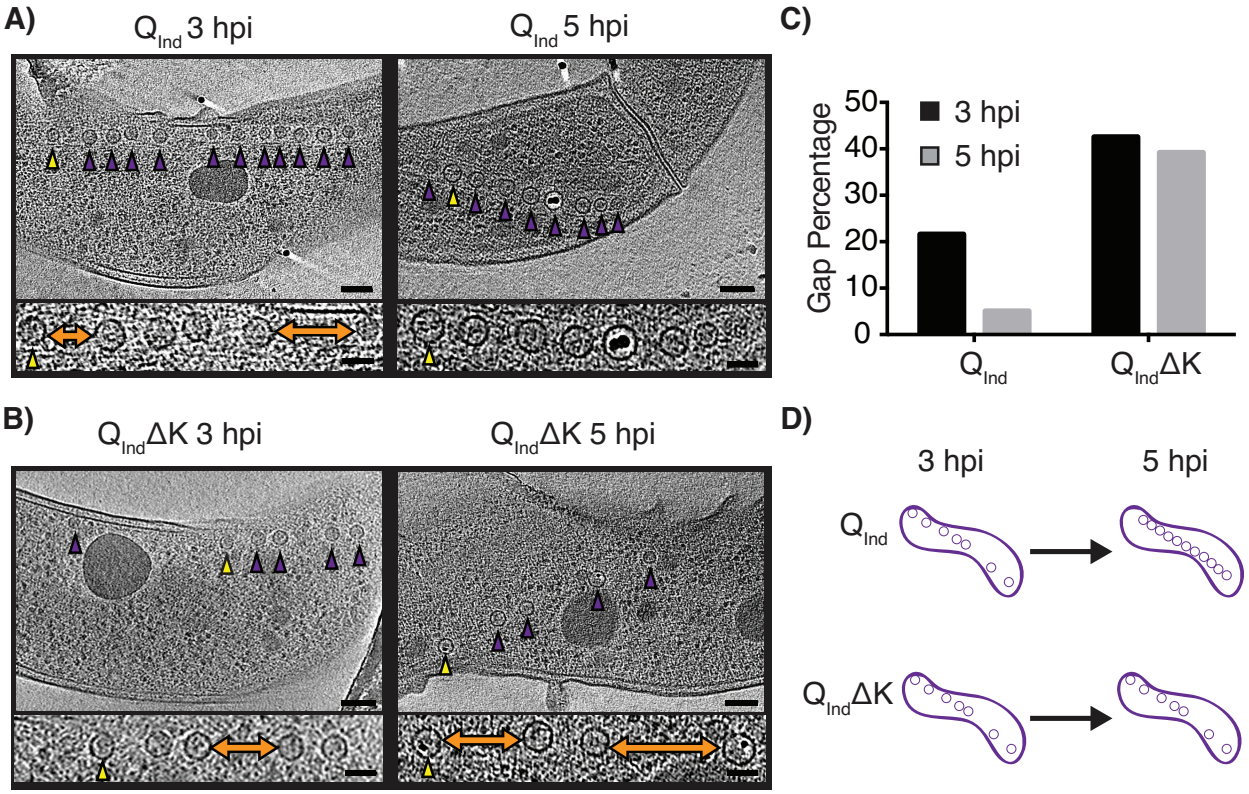

Figure 2: MamK is required for chain continuity, but not long-range alignment.
(A and B) Representative ECT images of long-range alignment of the magnetosome chain at 3 hpi and at 5 hpi for Q_{Ind} and Q_{Ind}ΔK respectively (scale bar = 100nm). Inset is a higher magnification of the same cell to show where gaps occur in the chain (scale bar = 50 nm). Gaps are denoted by double-sided orange arrows. Yellow arrowhead denotes the same magnetosome at each magnification for reference. Purple arrowheads point to individual magnetosomes in the chain. (C) Quantification of the number of gaps found in magnetosomes chains of induced Q_{Ind} and Q_{Ind}ΔK at 3 hpi and 5 hpi. Gap percentage is the percentage of edge-to-edge distances between adjacent and aligned magnetosomes >75 nm in length. The total number of edge-to-edge distances measured (n) for each timepoint are as follows: Q_{Ind} 3 hpi, n=74; Q_{Ind} 5 hpi, n=99; Q_{Ind}ΔK 3 hpi, n=94; Q_{Ind}ΔK 5 hpi, n=97) (D) Cartoon depicting magnetosome chain organization in Q_{Ind} versus Q_{Ind}ΔK. At 3 hpi, both strains exhibit long range, but discontinuous magnetosome alignment. At 5 hpi Q_{Ind} strain has filled these gaps, whereas Q_{Ind}ΔK does not fill the chain discontinuities.

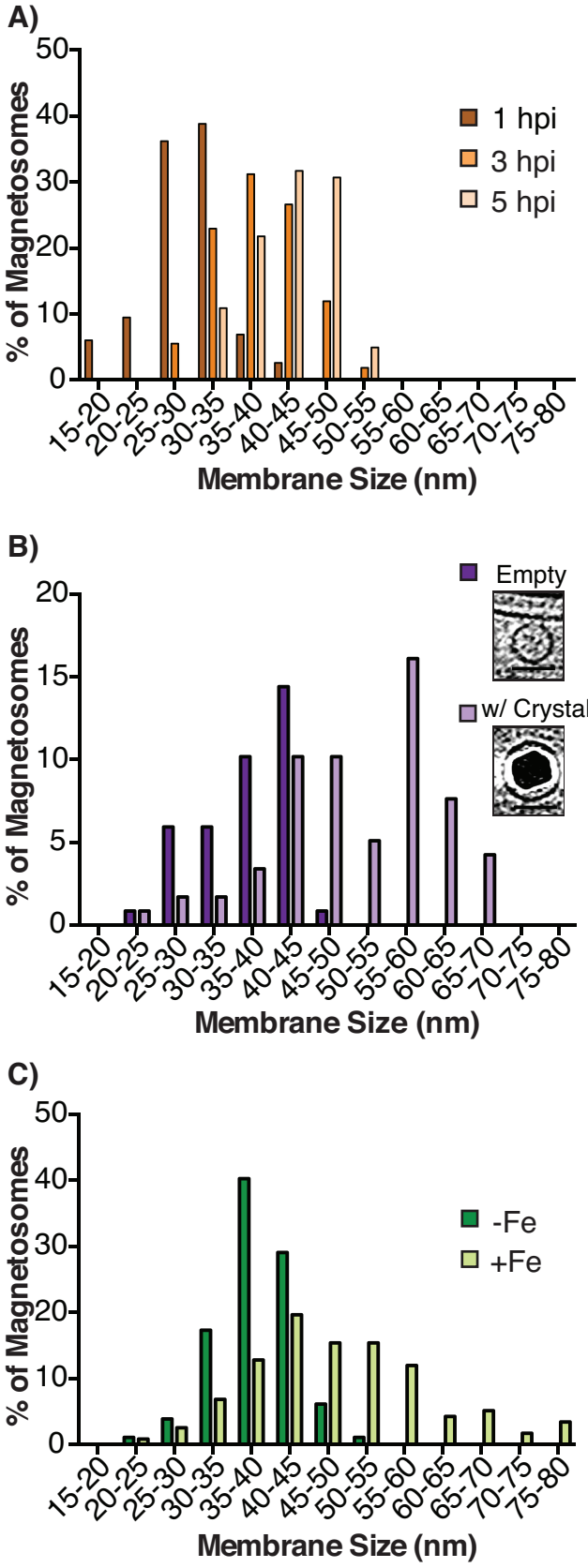

Figure 3: Magnetosome membranes grow in diameter in a manner that is dependent on their biomineralization state. (A) Distribution of magnetosome size at three points in the induction time course of Q_{Ind}, 1 hpi (n= 116), 3 hpi (n=110) and 5 hpi (n=101). (B) Distribution of magnetosome size in wildtype AMB-1 (n=117). Representative images of empty magnetosome versus magnetosome with crystal (scale bar = 50nm). (C) Magnetosome membrane size distribution in wildtype AMB-1 grown either in iron-rich (+Fe, n=117 magnetosomes) or iron-poor (-Fe, n= 172 magnetosomes). Membrane size is an average of 3 independent diameter measurements of the same magnetosome at the tomographic slice where it is largest and most visible.

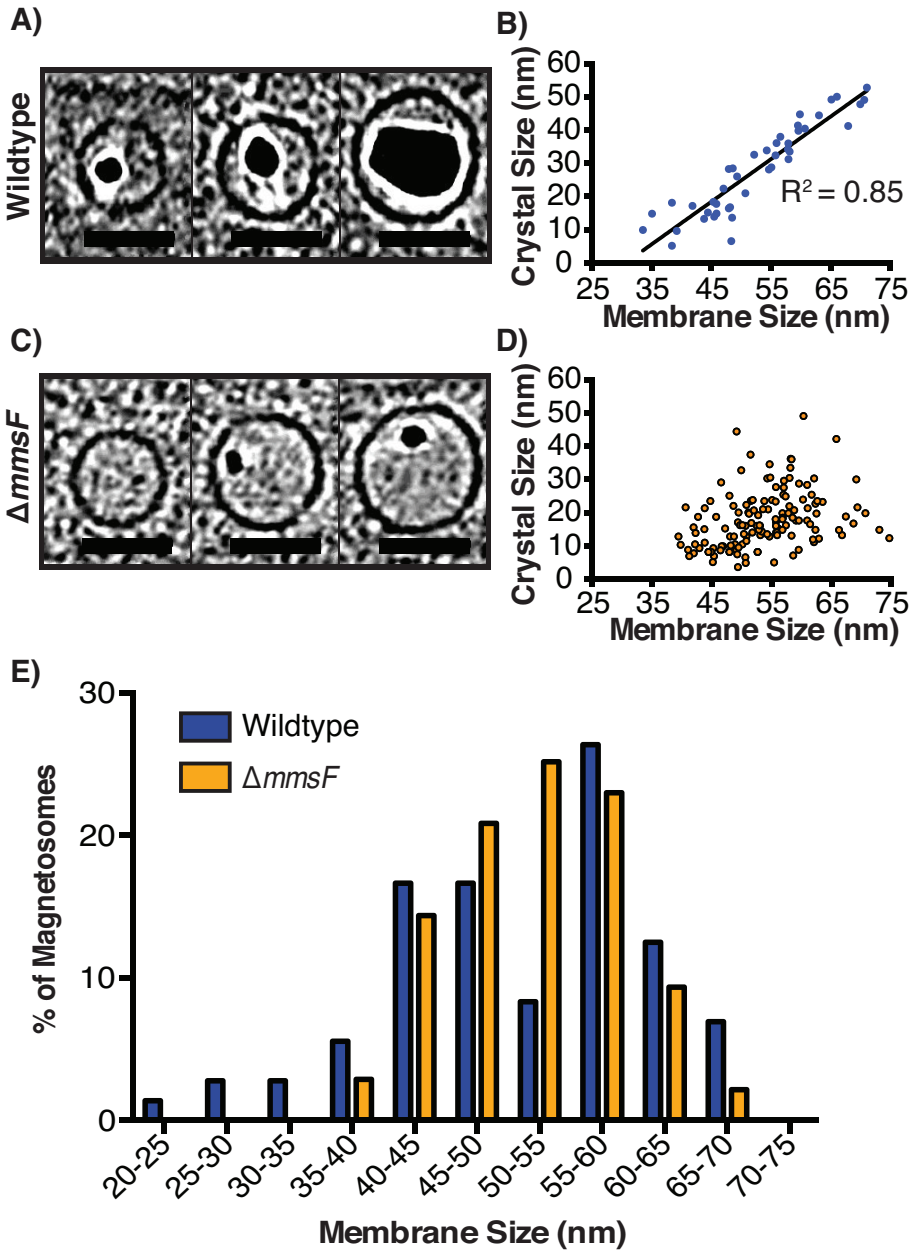

Figure 4: Crystal growth does not physically expand the magnetosome membrane. (A) Representative ECT images of magnetosomes of different sizes in wildtype AMB-1 (scale bar = 50 nm). (B) Scatter plot and regression analysis of membrane size versus crystal size for magnetosomes that harbor crystals in wildtype AMB-1 (n= 72 magnetosomes). The long axis (crystal length) is reported as crystal size. (C) Representative ECT images of magnetosomes of different sizes in wildtype Δ*mmsF* (scale bar = 50 nm). (D) Scatter plot of membrane size versus crystal size for magnetosomes that harbor crystals in Δ*mmsF* (n= 140 magnetosomes). The long axis (crystal length) is reported as crystal size. (E) Distribution of magnetosome size in Δ*mmsF* (n=243) compared to wildtype AMB-1 (n=117).

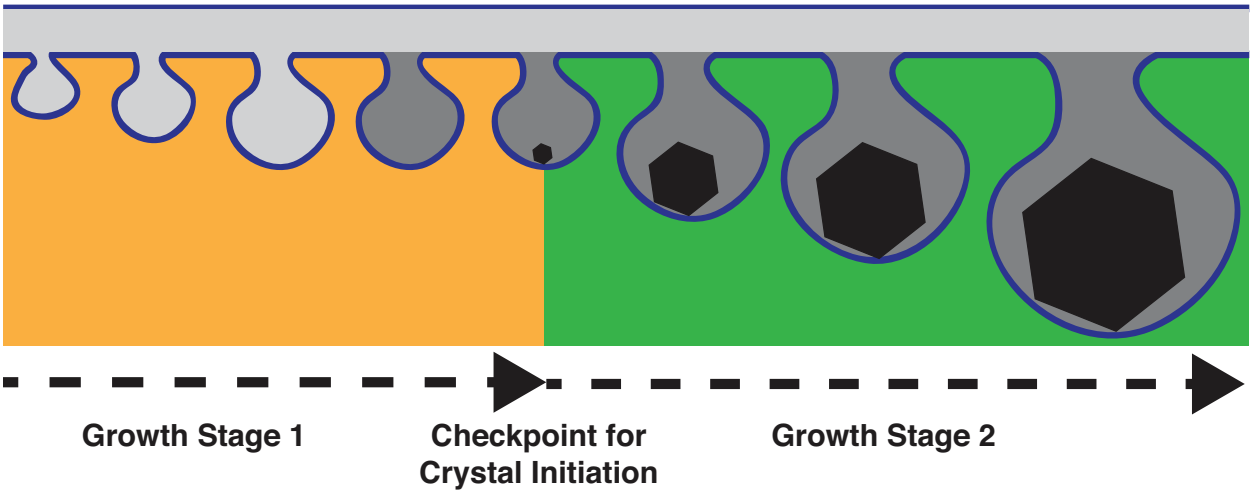

Figure 5: Magnetosome membrane growth is a two-step growth mechanism dependent on biomineralization. The magnetosome membrane compartment is remodeled in two growth stages. In the first stage (orange), the inner membrane is remodeled to form the magnetosome compartment. The magnetosome lumen is most likely similar to that of the periplasm (light grey). Membrane size is restrited until conditions inside the magnetosome membrane are optimal for biomineralizaiton (dark grey). Crystal initiation triggers a second growth phase (green) to accommodate a growing crystal.

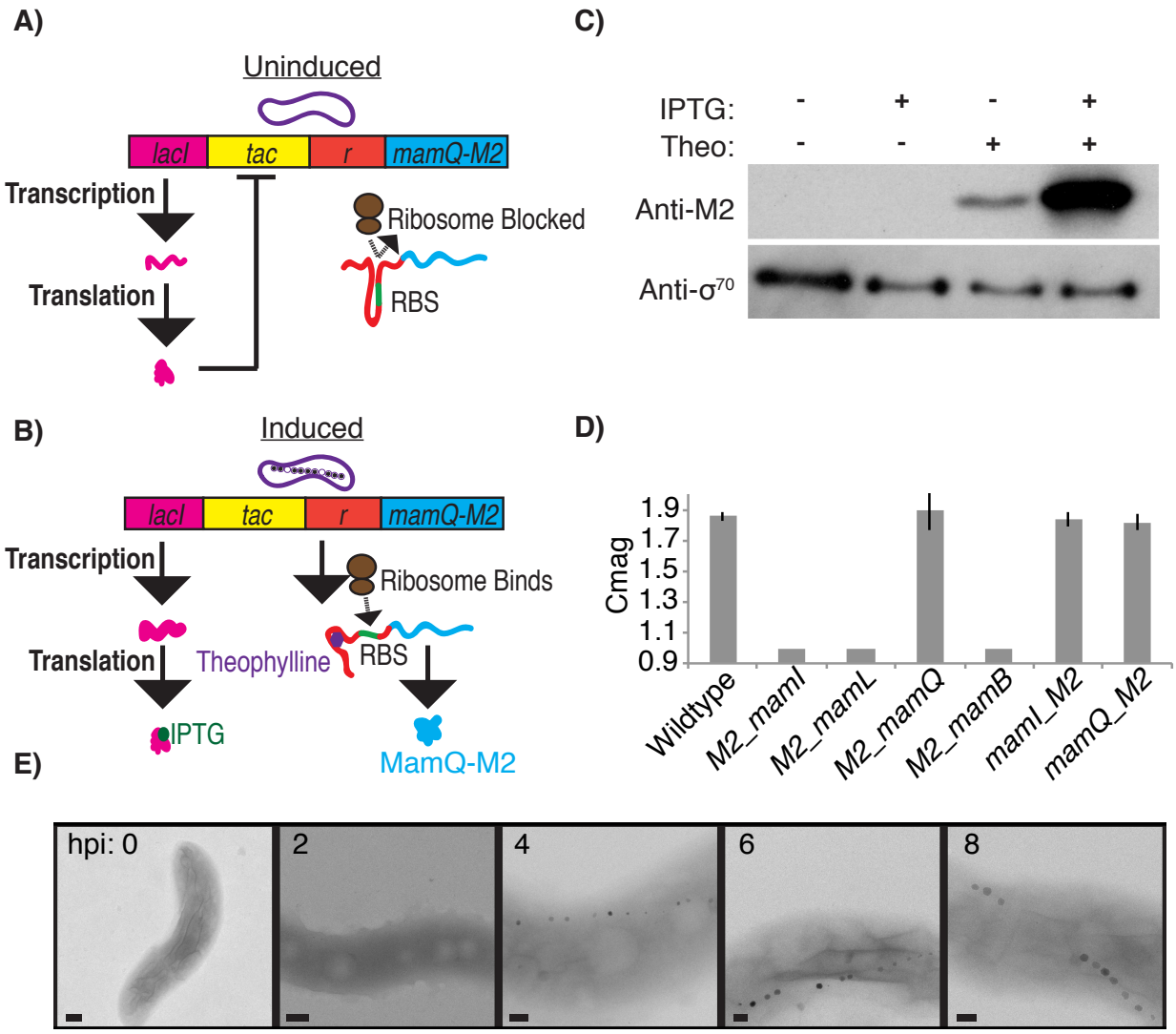

Figure S1. Inducing magnetosome formation in AMB-1 LD9ΔQ strain (A and B) Schematic illustrating how the combination of *lacI* and a riboswitch provides transcriptional and post-transcriptional control over mamQ-M2. (A) LacI blocks transcription from the *tac* promoter and the riboswitch (r) blocks translation (RBS - ribosome binding site) of *mamQ-M2* that could result from low level, leaky transcription. (B) Transcriptional inhibition by LacI is relieved by the addition of IPTG and post-transcriptional inhibition by the riboswitch is relieved by the addition of theophylline. (C) Western blot for MamQ-M2 (35 kD) expression in uniduced, partially induced, and fully induced state. Cultures were grown 24 hours in either the presence or absence of inducers. Anti-M2 antibody was used to probe for MamQ-M2 and Anti-σ70 antibody was used to probe for loading control. (D) M2 translational fusion to the N-terminus or C-terminus of *mamI, mamL, mamQ* and *mamB* in their respective deletion backgrounds (Δ*mamI*, Δ*mamL*, LD9Δ*mamQ*, LD9Δ*mamB*). Mating of C-terminal M2 tagged version of *mamL* and *mamB* into AMB-1 was unsuccessful. Complementation is assessed by the coefficient of magnetism (Cmag) of the cell culture. (E) Representative transmission electron microscopy (TEM) images of biomineralization throughout the induction time course. Cells imaged at 0, 2, 4, 6 and 8 hours post-induction (hpi) (Scale bar =200 nm).

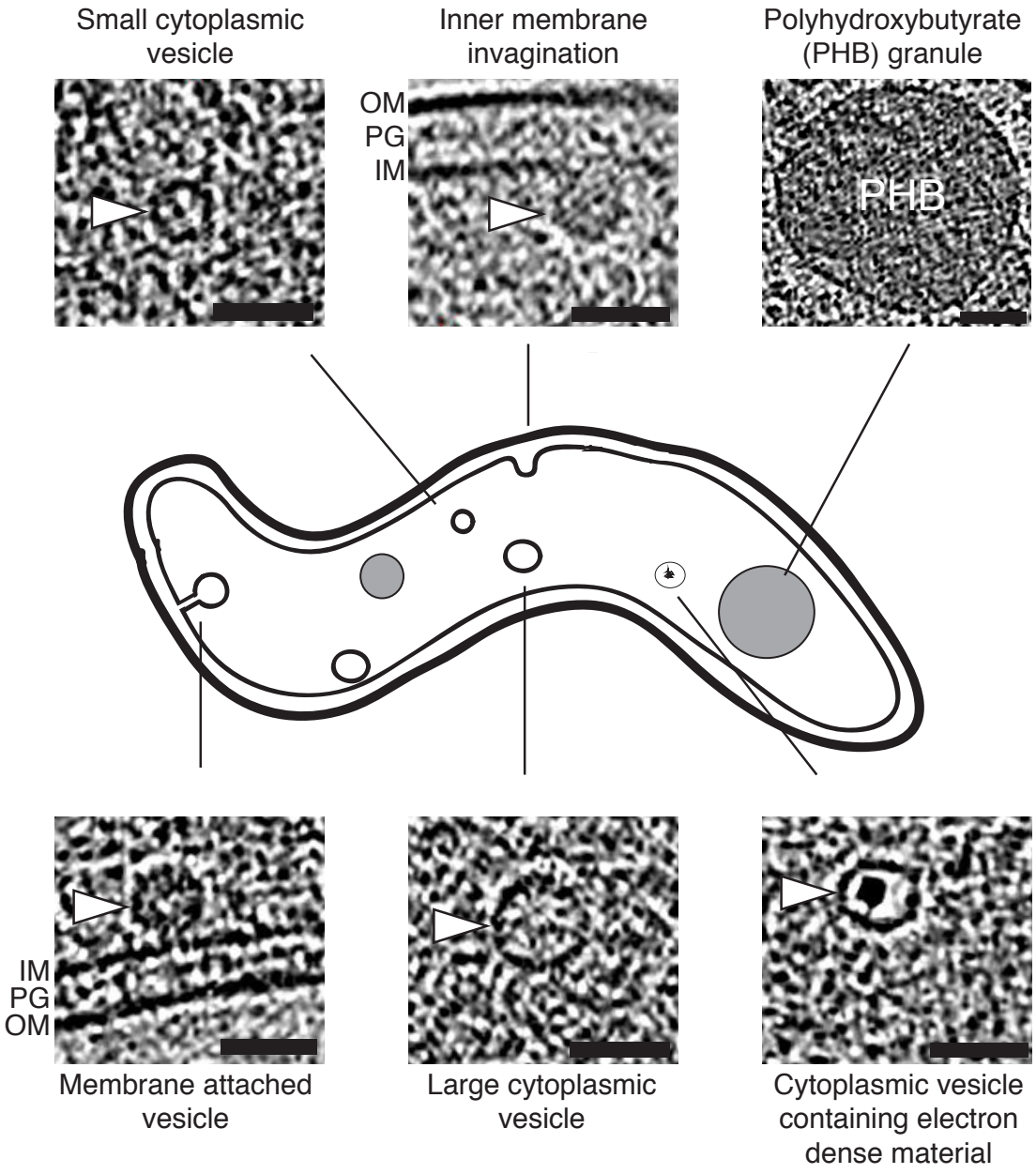

Figure S2. Isolated magnetosome-like structures found in LD9ΔQ and uninduced Q_{Ind}. Representative ECT images of membrane invaginations, cytoplasmic vesicles of different sizes, vesicles containing electron dense material, polyhydroxybutyrate (PHB) granule, and vesicles that are connected to the inner membrane by a tiny neck. Inner membrane (IM), peptidoglycan cell wall (PG) and outer membrane (OM) are labeled accordingly. Structures indicate by white arrowheads, (scale bar = 50 nm).

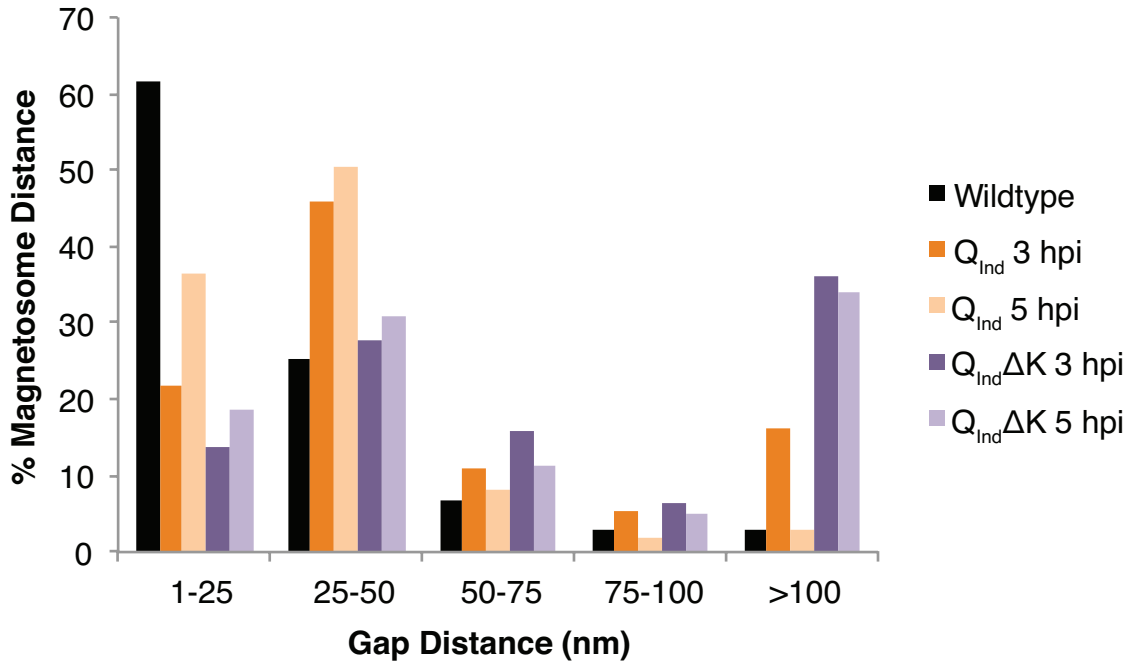

Figure S3. Histogram of measured edge-to-edge distance between adjacent magnetosomes. Wildtype, n =130; Q_{Ind} 3 hpi, n =74; Q_{Ind} 5 hpi, N =99; $Q_{Ind}\Delta K$ 3 hpi, n =94; $Q_{Ind}\Delta K$ 5 hpi, n =97)

A)

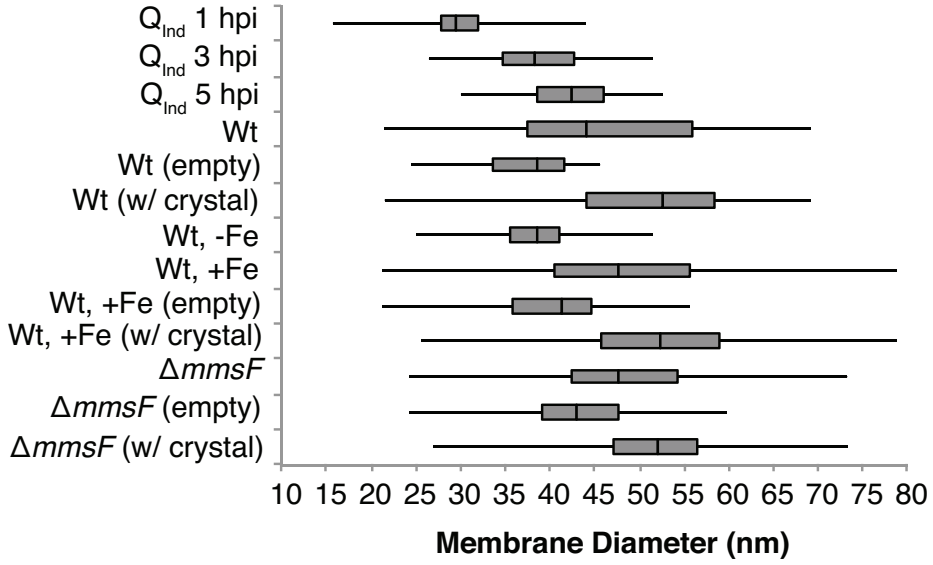

B)

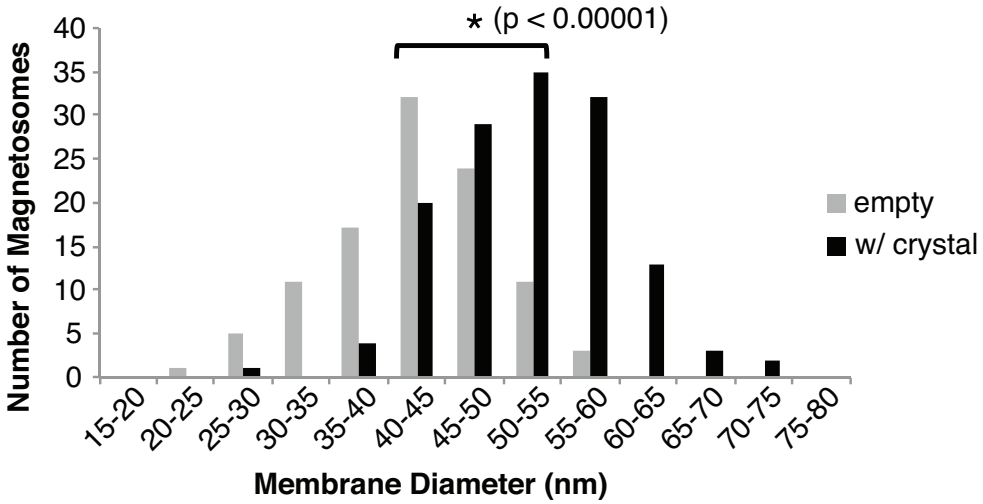

Figure S4. (A) Summary of membrane diameter distributions. (B) Distribution of membrane diameter for *ΔmmsF* (n=243) indicating that magnetosomes of *ΔmmsF* that have not initiated biomineralization are also growth-limited. (*) Indicates results of two- tailed student t-test.

Strain, condition	n	Mean ± s.d.	Median	Min	Max	Q1	Q3	Figure
Q_{Ind} 1 hpi	116	29.41 ± 5.04	29.40	15.80	44	27.75	32	3A
Q_{Ind} 3 hpi	109	38.51 ± 5.54	38.20	26.50	51.60	34.80	42.60	3A
Q_{Ind} 5 hpi	101	42.28 ± 5.17	42.53	30.01	52.60	38.60	46.03	3A
Wt	117	45.70 ± 11.43	44.02	21.61	69.21	37.48	55.87	3B, 4E
Wt (empty)	45	36.94 ± 5.92	38.42	24.52	45.61	33.67	41.51	3B, 4E
Wt (w/ crystal)	72	51.18 ± 10.61	52.48	21.61	69.21	44.10	58.44	3B, 4B
Wt, -Fe	170	38.22 ± 4.72	38.58	24.94	51.58	35.64	41.11	3C
Wt, +Fe	117	48.52 ± 11.74	47.68	21.22	78.85	40.60	55.60	3C
Wt, +Fe (empty)	43	40.33 ± 7.25	41.43	21.22	55.60	35.93	44.70	3C
Wt, +Fe (w/ crystal)	74	53.27 ± 11.23	52.42	25.6	78.85	45.81	59.02	3C
Δ*mmsF*	243	47.89 ± 8.59	47.67	24.29	73.32	42.32	54.18	4E
Δ*mmsF* (empty)	104	42.43 ± 7.03	42.99	24.29	59.78	39.03	47.62	S4B
Δ*mmsF* (w/ crystal)	139	51.97 ± 7.30	52.10	27.11	73.32	47.04	56.40	S4B

Table S1. Membrane diameter distribution characteristics. Mean and standard deviation (s.d), minimum (min), maximum (max), first quartile (Q1), third quartile (Q3) and number of magnetosomes measured (n) for each strain/condition in this study. Strains include: inducible strain (Q_{Ind}), wildtype AMB-1 (Wt) and Δ*mmsF*. Conditions include hours post induction (hpi), iron-rich (+Fe) or iron-poor conditions (-Fe). The biomineralization state (empty or with crystal) of the magnetosomes measured in a given strain/condition is noted in parenthesis. Figure number for distribution is indicated in the far right column. All mean values reported in the main text are reported with standard deviations.

Strain, Condition	U-Value	Z-score	P-value	T-Value	P-value
Q_{Ind} 1 hpi vs. 3 hpi	1357.5	-10.22	<0.00001	12.96	<0.00001
Q_{Ind} 1 hpi vs. 5 hpi	440	-11.74	<0.00001	18.54	<0.00001
Q_{Ind} 3 hpi vs. 5 hpi	3495.5	-4.65	<0.00001	2.74	0.006743
Wt empty vs. w/ crystal	382	6.93	<0.00001	8.23	<0.00001
Wt, +Fe empty vs. w/ crystal	516.5	6.07	<0.00001	6.77	<0.00001
Wt -Fe vs. +Fe	4140	-8.45	<0.00001	10.31	<0.00001

Table S2. Statistical significance test of membrane diameter distributions between two groups. Mann-Whitney U-test, two tailed (orange) tests null hypothesis that the the median of both populations are equal (H.B. Mann, D.R. Whitney, Ann Math Stat 18:50–60, 1947, doi: 10.1214/aoms/1177730491). Student T-test, two tailed (blue) tests null hypothesis that the mean of both populations are equal.

Table S3. List of plasmids

Plasmid	Description	Plasmid backbone
pAK0	suicide vector	Reference (67)
pAK605	vector to integrate into intergenic region of *amb0397*	pAK31
pAK701*	N-terminal M2 tag	pAK605
pAK702*	C-terminal M2 tag	pAK605
pAK728	*M2-mamI*	pAK701
pAK729	*M2-mamL*	pAK701
pAK730	*M2-mamQ*	pAK701
pAK735	*M2-mamB*	pAK701
pAK731	*mamI-M2*	pAK702
pAK734	*mamL-M2*	pAK702
pAK732	*mamQ-M2*	pAK702
pAK733	*mamB-M2*	pAK702
pAK550	riboswitch *mamK*	Reference (76)
pAK312	*lacI, mamL*	pBBR vector
pAK892	riboswitch, *mamL*	pAK550
pAK893	*lacI*, riboswitch, *mamL*	pAK892
pAK894	SwaI site between *tac* promoter and riboswitch	pAK893
pAK895	contains tight binding *lac* operator	pAK894
pAK741	inducing module, *mms16* promoter (reverse)	pAK605
pAK748	inducing module, *mamQ-M2*, *mms16* promoter (reverse)	pAK741
pAK897	*gfp-mmsF* allelic replacement	pAK31
pAK54	*mms16* promoter	pBBR vector

*Plasmid constructed by Patrick Browne

Table S4. List of Strains

Strain	Description	Reference
AK30	AMB-1 wildtype	Reference (98)
AK169	AMB-1_ *gfp-mmsF* (allelic replacement)	this work
AK46	*amb0972* and *amb1002-amb1007* deleted (LD9ΔQ)	Reference (33)
AK168	LD9ΔQ_*gfp-mmsF*	this work
AK167	Q_{Ind}: AK168 with *mamQ-M2* inducible plasmid (pAK748) integrated into the intergenic region between *amb0397* and *amb0398*	this work
AK166	deletion of *mamK* (amb0965) in AK46	this work
AK202	AK166 with *gfp-mmsF* allelic replacement	this work
AK203	Q_{Ind}ΔK: AK202 with *mamQ-M2* inducible plasmid (pAK748) integrated into the intergenic region between *amb0397* and *amb0398*	this work

Table S5. List of primers

oAK #	Target	Sequence
C75	*M2-mamI*	acacaggatccccaagcgtgattttcggactgc
D05	*M2-mamI*	tgtgtgcggccgctcaaccatcgatgtcaggg
D04	*mamI-M2*	acacaactagtatgccaagcgtgattttcgg
C77	*mamI-M2*	tgtgtggatccaccatcgatgtcagggtctgaag
C73	*M2-mamL*	acacaggatccgtaagattgatcggatcgttgg
C61	*M2-mamL*	tgtgtgcggccgctcagcgcttgatgacgatg
5SpeL*	*mamL-M2*	ggactagtatggtaagattgatcggatcgttgg
C50	*mamL-M2*	tgtgtggatccgcgcttgatgacgatgctcttc
C74	*M2-mamQ*	acacaggatccgcattaggcgacgcgaatgttgg
C62	*M2-mamQ*	tgtgtgcggccgctcatttcttgatgtcctgcgcatg
5SpeQ*	*mamQ-M2*	ggactagtatggcattaggcgacgcg
C51	*mamQ-M2*	tgtgtggatcctttcttgatgtcctgcgc
C76	*M2-mamB*	acacaggatccaccctgttcaaggggtcc
D02	*M2-mamB*	tgtgtgcggccgctcaggcccgtgccgcg
D03	*mamB-M2*	acacaactagtatgaccctgttcaaggggtcctcg
C78	*mamB-M2*	tgtgtggatccggcccgtgccgcggc
5EcoL	*mamL*	ggcgaattcatggtaagattgatcggatc
3SpeL	*mamL*	ggactagttcagcgcttgatgacgatg
D25	*lacI*	caaaagctgggtaccgggcccccccaagctttggtgcaaaacctttcgcgg

Table S5. List of primers (continued)

oAK #	Target	Sequence
D28	*lacI*	cgatgattaattgtcaacagctcctcgagcattgcgttgcgctcactg
C19	*tac* promoter	cggctcgtataatgtgtatttaaatgctaacaagtctagcgaaccgc
C20	*tac* promoter	gcggttcgctagacttgttagcatttaaatacacattatacgagccg
C21	*tac* promoter	acacaatttaaataattgtgagcgctcacaattcacacattatacgagccg
D10	riboswitch	tgtgtactagtcatcttgttgatacccccctgcgcagcg
D13	*lacI*	acacaagatcttggtgcaaaaccttcgcggtatgg
D62	*mms16* promoter	ctggagctccaccgcggtggcggccatcaccgtctgtgcgccggg
D63	*mms16* promoter	gacggactagttctagagcggccgcgttattcctccaacccgggg
E07	*mamQ*	gcaggggtatcaacaagatgactagtatggcattaggcgacgcgaatg
E12	M2	gcggccgctctagaactagttcacttgtcgtcgtcgtccttgtagt
F02	*amb0956*	tcctgcagcccgggggatccactagtggccatgactctacactccgaatc
F03	*amb0956*	ctccagtgaaaagttcttctcctttactcattccccccctcctcctcgttc
F04	*amb0957* downstream intergenic region	gcggcggccaaagcagcagcgggatccactgaagctatccttcgcagcac
F05	*amb0957* downstream intergenic region	caccgcggtggcggccgctctagaactagttggcgccagcttgtcgg
E69	*gfp* (mutant 3)	atgagtaaaggagaagaacttttcactggag
E70	*gfp* (mutant 3)	ggatcccgctgctgctttg

*Primer designed by Dorothée Murat

CHAPTER 3

Subcellular organization and magnetosome positioning in *Magnetospirillum magneticum* AMB-1 (unpublished data)

Elias Cornejo and Hayley McClausland

Department of Plant and Microbial Biology, University of California, Berkeley, CA, USA

ABSTRACT

The subcellular positioning of organelles in bacteria is vital for both the function and faithful segregation of organelles amongst daughter cells (4, 46). *Magnetospirillum magneticum* AMB-1 synthesizes magnetic crystals inside membrane-bound compartments called magnetosomes (99). Individual magnetosomes are organized into a chain across the cell, which gives the bacterium the remarkable ability to passively align to external magnetic fields (50). This subcellular feature is thought to provide a selective advantage in nature by assisting in navigation to find the proper redox environment in the water column (100). However, exactly how the magnetosome chain is segregated and maintained is still unknown. Here we employ a pulse-chase strategy and establish a novel magnetosome marker that can distinctly label old versus new magnetosomes. We show that these two populations of magnetosomes can be labeled in an actively growing cell culture. By time-lapse imaging, we show how this strategy could be used to follow magnetosome chain segregation and to identify the sites of magnetosome biogenesis. Once optimized, this technique can shed light on how subcellular organization and positioning of magnetosomes is maintained over multiple cell generations.

INTRODUCTION

The ultimate goal of this work is to understand the cell biological mechanisms of bacterial organelle formation using the magnetosome organelles of magnetotactic bacteria. We would like to know how these organisms produce magnetic crystals inside of membrane-bound organelles and align them in a chain across the cell. Previous genetic and biochemical studies have revealed that magnetosome formation can be separated into distinct developmental stages: membrane formation, chain organization, and crystal biomineralization (33). However, it is difficult to study any one of these developmental stages in wildtype AMB-1, since the individual magnetosomes in a chain are at different stages of development. Therefore, understanding how these seemingly separate developmental stages of magnetosome formation fit together in a dynamic *in vivo* system is a major challenge facing researchers in the field.

To circumvent the issues with studying magnetosome formation in wildtype, we designed a genetic system to have inducible control over the developmental stages of magnetosome formation (101). We found that newly formed magnetosomes self-organize into a chain in two distinct stages. First, clusters of magnetosomes, separated by several gaps, align across the length of the cell. Next, powered by the action of the actin-like protein MamK, the discontinuities in the chain are repaired and a coherent magnetosome chain is formed. Although the later stages of chain formation could be resolved by the inducible system, our strict criteria for distinguishing newly formed magnetosomes from other membrane structures also present in the cell made characterizing the early stages of chain formation difficult. Nonetheless, in the early stages of magnetosome biogenesis, magnetosome clusters did not appear to be restricted to a particular cellular location. Recently, a similar study used an inducible system to track *de novo* magnetosome biogenesis and chain formation in a closely related magnetotactic bacterium, Magnetospirillum gryphiswaldense MSR-1(102). This study also could not find a predictable pattern to magnetosome biogenesis. Therefore, it seems that when magnetosome formation is induced in the absence of a pre-existing chain, magnetosomes are capable of forming anywhere in the cell and this seemingly stochastic pattern of formation somehow coalesce into a chain.

Once a magnetosome chain is formed, it appears to serve as a cellular landmark for magnetosome biogenesis. In wildtype cells or magnetosome induced cells that have formed chains, the presence of unaligned, randomly-positioned magnetosomes are rare; the vast majority of magnetosomes appear to form in line with the established magnetosome chain (5). Therefore, although the inducible system offers several advantages to controlling and capturing the early membrane remodeling events that occur to form magnetosomes, it may not reflect the actual positioning of newly formed magnetosomes of wildtype AMB-1. In wildtype AMB-1, the magnetosome chain is divided, segregated and maintained amongst daughter cells, thus the plane of alignment seems to be always established. Presumably, magnetosome age can be inferred from the size and shape of the crystals – that is, the oldest magnetosomes should have the largest crystals, while the newest magnetosomes are those that are devoid of crystals. Surprisingly, there is not a readily identifiable pattern of empty vs. full magnetosomes in the chain. This could be due to a stochastic positioning of new magnetosomes within the chain; alternatively, if new magnetosomes are consistently added to the same position within the chain, such as on the ends, this may be occluded as magnetosome chain is divided and segregated and maintained over multiple cell generations.

Being able to track magnetosomes within the chain will allow the researchers in the field to better study an individual magnetosome as it progresses through its developmental stages of membrane remodeling, alignment, and biomineralization. Furthermore, this could help resolve whether proteins are differentially targeted to the magnetosome at different developmental stages. The experiments outlined below aim to identify the sites of magnetosome biogenesis in wildtype AMB-1 by (1) differentially labeling pre-existing vs. newly made magnetosomes over time, (2) determining whether a magnetosome protein can be targeted to pre-existing magnetosomes and (3) determining if a magnetosome membrane protein can diffuse into adjacent magnetosomes.

MATERIALS & METHODS

Staining and Imaging of Halo-tagged proteins

JF 549 and JF 646 Halo ligands were obtained from Luke Lavis's lab at HHMI Janelia. Research Campus. Ligands were received as 100 nmol of dried power. A 5 mM stock was prepared by re-suspending the powder in 20 microliters of dimethyl sulfoxide (DMSO). AMB-1 cells transformed with a plasmid expressing halo-tagged proteins were stained with 5 μM of Halo-ligand diluted in MG media (note: it is possible to stain the cells with as low as 300 nM of halo-ligand).

Cells were grown to an OD_{400} of ~0.250. 1 mL of cells was centrifuged at 16000 x g for 3 minutes. Cell pellet was re-suspended in 100 μL of 5 uM Halo-ligand, protected from light and incubated at 30 °C for 15 minutes. Cells were washed 3 times by first centrifuging at 16000 x g for 1 minute and then re-suspending the cell pellet in 100 μL of MG media (note: Halo-ligand stain and subsequent washes were removed with a pipette and treated as DMSO waste).

The excitation/emission of JF 549 is 549 nm /571 nm respectively and can be imaged using a standard Rhodamine or Texas Red Filter. The excitation/emission of JF 646 is 646 nm/ 664 nm respectively and can be imaged using a standard Cy5 filter set. However, JF 646 can be excited by the most standard Rhodamine and TR filter sets; therefore, for two color imaging using both JF 549 and JF 646 halo ligands, JF 549 was visualized using the custom Cy3/TRITC filter cube(Chroma, Catalog #: 49004) and JF 646 was imaged using the Cy5 filter cube.

Pulse-Chase

For pulse-chase experiments, a 50 mL culture was inoculated 1:100 from a stock culture and incubated at 30 °C for 48 hrs. The 50 mL culture was centrifuged at 8000 x g for 10 minutes. The cell pellet was re-suspended in 500 μL of 5 μM JF 549 (diluted in MG media) and transferred to a 1.5 mL eppendorf tube. Cells were protected from light and incubated at 30 °C for 15 minutes. Cells were washed 3 times by first centrifuging at 16000 x g for 1 minute and then re-suspending the cell pellet in 500 μL of MG media. After 3 washes, cells were re-suspended in 10 mL of MG. An aliquot of cells was further diluted to measure optical density in the accurate range. Cells were then sub-cultured into 10 mL cultures at range of optical densities

(OD400 = 0.01, 0.05., 0.1) and incubated 18-24 hours at 30 °C in a microaerobic chamber containing 10% oxygen. Optical density was measured to verify growth and Cmag. 1 mL of cell culture was removed and centrifuged at 1600 x g for 3 minutes. Cell pellet was re-suspended in 500 µL of 5 uM of JF 646 Halo-ligand. Staining procedure was the same as that for JF 549. Cells were re-suspended in 25 µL of MG media. 7 µL of cells were then immobilized on 1% (w/v) agarose pads containing MG medium. Cells were overlaid with a coverslip and sealed with hot liquid mixture of petroleum jelly, lanolin, and paraffin (1:1:1[w/w/w]) (VALAP). The sample was then imaged with a Zeiss AxioObserver Z1 equipped with a Hamamatsu 9100-13 EMCCD camera. JF 549 was visualized using the custom Chroma filter (Cat. #: 49004) and JF 646 was imaged using the Cy5 filter cube.

Fluorescence recovery after photobleaching (FRAP) and Fluorescence loss in photobleaching (FLIP) Experiments

Fluorescence recovery after photobleaching (FRAP) experiments were performed as previously described, using a laser scanning confocal microscope, Zeiss LCM710 (103). For fluorescence loss in photobleaching (FLIP) experiments, the laser intensity was set to 100% and samples were bleached with 20 iterations of 500 millisecond pulses per cycle for up to 15 cycles.

Time-lapse imaging using agarose pads and CellASIC microfluidics

Cell Culture
For time-lapse imaging, cells were inoculated from stock cultures 1:100 into 10 mL of MG media and incubated in microaerobic condition (10% oxygen) at 30 °C for 18-24 hours until the OD_{400} reached ~ 0.1. 1.5 mL of cells were centrifuged at 16000 x g for 3 minutes and cell pellet was re-suspended in 100 µL of MG media.

Agarose pads
0.7 g of agarose was added to 100 mL of MG media and melted in a microwave for 2 minutes to prepare 0.7% agarose/MG. Molten agarose/MG was allowed to cool to room temperature, then 980 µL of agarose/MG was added to a 1.5 mL eppendorf tube containing 10 µL of 100X iron malate and 100X vitamin solution, quickly vortexed, then immediately spotted on glass slide (~400 µL per slide). Another glass slide was immediately placed on top to create an "agarose sandwich" and allowed to set for 1 minute. Slides were carefully separated, agarose was cut to a square the size of the glass coverslip. 10 µL of cells was spotted on the agarose/MG pad and coverslip was sealed with (VALAP).

CellASIC™ ONIX Microfluidics System
Bacterial CellASIC™ ONIX B041-02 microfluidic plates were purchased from EMD Millipore. To prime the plate, PBS solution was vacuum suctioned out of each well and replaced with MG media (300 µL per well). Plate was then sealed using CellASIC™ ONIX microfluidics chamber and MG media was flowed through well 8 for 15 minutes, then through wells 1-6 for 45 minutes at 2.5 psi (~4 microliters/hour). After 1 hour of priming, the plate was unsealed and 25 µL of cells were added to well 8. Cells were loaded into the chamber by flowing V8 are 2 psi and 12 seconds to prime the cells for loading, followed by flowing V8 and V6 at 4 psi for 6 seconds to

trap the cells. This loading protocol was repeated until the desired cell density was trapped. Cells are typically trapped at steps 4 and 5 of the microfluidic plate. Once loaded, a constant flow rate of 2.5 psi was maintained.

Imaging
Time-lapse images were acquired using the Zeiss AxioObserver Z1 equipped with a Hamamatsu 9100-13 EMCCD camera in the biological imaging facility at the University of California, Berkeley. Images were acquired using iVision Multi-D program. Fluorescence images of cells stained with JF 549 were acquired using a custom filter cube manufactured from Chroma (Cat #: 49004).

Plasmid construction

A plasmid encoding the full length *halo* tag (mHalo, pAK969) was gifted by Liam Holt's lab from the University of California, Berkeley. Full length *halo* was amplified off of pAK969 using oligos EC166 and EC167 and cloned into EcoRI and SpeI sites of pAK22 and pAK54 to in order to place halo under the control of the *tac* promoter (pAK976) and the *mms16* (pAK977) promoter respectively. For N-terminal *halo* tag (pAK978), the *halo* tag was amplified excluding its stop codon using oligos EC166 and EC151 and cloned into EcoRI and SpeI sites of pAK54. For C-terminal *halo* tag (pAK979), the *halo* tag was amplified excluding its start codon using oligos EC152 and EC167 and cloned into EcoRI and SpeI sites of pAK54. In order to construct *halo-mmsF* (pAK983), *mmsF* with its N-terminal flexible linker was amplified off of pAK532 using oligos EC and EC and cloned into the SpeI site of pAK978.

RESULTS

In order to differentially label pre-existing versus newly formed magnetosomes, we devised a pulse-chase system in AMB-1 using Halo-tagged magnetosome proteins. Halo tag is a commercially available modified halogenase enzyme that covalently binds a variety of ligands (104). The halo ligands are attached to a variety of different fluorophores or biochemical tags. For our purposes, we obtained two halo ligands, JF549 and JF646, which are synthesized with two distinct fluorophores whose excitation/emission would allow for dual labeling and imaging (Figure 1A and 1B) (105). We empirically determined that the standard Rhodamine filter set that is used to image JF 549 also excites the JF646 ligand and therefore is not suitable for dual labeling experiments (data not shown). To circumvent this issue we designed a custom filter set that is equipped with a band-pass emission filter instead of a long-pass emission filter that can image JF549 without imaging the emitted JF646 fluorescence (Figure 1A and 1B).

An N-terminal transcriptional halo tag fusion to *mmsF* was cloned and transformed in to wildtype AMB-1. This Halo-tagged protein appears to be a functional fusion as assessed by correct localization (Figure 1C). Visually tacking magnetosome biogenesis using JF 549 and JF 646 to pulse-chase label Halo-MmsF in wildtype relies on the assumption that Halo-MmsF cannot freely diffuse between magnetosomes. If magnetosome proteins freely diffuse between adjacent magnetosomes, then a Halo-MmsF would not stably mark the position of pre-existing magnetosomes after the pulse label. Therefore, we first had to characterize the protein dynamics

of labeled Halo-mmsF before we could confidently track new and old populations of magnetosomes using these proteins.

In order to address whether Halo-MmsF can freely diffuse between magnetosomes, we performed a fluorescence recovery after photobleaching (FRAP) experiment on cells stained with JF549. Fluorescence recovery in the photo-bleached region would indicate that Halo-MmsF from unbleached regions could diffuse into the bleached region of the magnetosome chain. We found that Halo-MmsF pulse-labeled with JF549 shows no recovery of the bleached region even after 20 minutes (Figure 2A). Alternatively, if Halo-MmsF is a dynamic protein, then fluorescence loss in photobleaching (FLIP) which iteratively bleaches the same location, would eventually bleach the entire pool of Halo-MmsF. Our FLIP experiments with Halo-MmsF in wildtype are consistent with the dynamics of a non-diffusible magnetosome proteins (Figure 2B). Although it is still possible that Halo-MmsF diffuses on longer time scales, this is not typical of diffusible membrane proteins, which have exhibited recovery within a timeframe of 10 seconds (106).

To explore whether the magnetosome membrane itself, confines the movement of Halo-MmsF, we also performed FRAP and FLIP on pulse-labeled Halo-MmsF in the ΔMAI strain which lacks magnetosomes. In this genetic background, we were unable to photo-bleach Halo-MmsF by either FRAP or FLIP (data not shown). The FRAP results would suggests that there is extremely rapid fluorescence recovery, however, these dynamics were not reflected in the inability to photobleach the entire cell by FLIP. This suggests that optimizing the fluorescence intensity and the number of iterations for photobleaching are required to better characterize Halo-MmsF dynamics in the ΔMAI strain.

The above experiments suggest that Halo-MmsF can be efficiently pulse-labeled and does not diffuse between magnetosomes. Since Halo-MmsF remains stably associated with the magnetosomes to which it is initially targeted, we can use it to distinguish between pre-existing versus newly made magnetosomes. In order to follow pre-existing magnetosomes, wildtype AMB-1 transformed with a plasmid expressing Halo-MmsF, were pulse-labeled with JF 549. To identify the newly, made magnetosomes, pulse-labeled cells were passaged and grown overnight, then chase-labeled with JF646. Clear distinct patches of pulse labeled versus chase-labeled magnetosomes were observed after outgrowth (Figure 3). We could not determine a distinct pattern of where newly made magnetosomes are incorporated into the pre-existing magnetosome chain. However, it appears that the pulse-label remains stably associated with the pre-existing magnetosome population, since increasing the number of cell division that cells are allowed to undergo decreases the number of foci per cell (Figure 4A and 4B). These preliminary results suggest that the Halo-tagged proteins can be used to confidently label pre-existing versus newly synthesized magnetosomes. However, further control experiments are required to verify that the initial pulse with JF549 completely labeled the pre-existing are required to ensure that the JF656 chase-labeled magnetosomes are not a result of incomplete pulse-labeling.

In order to gain better spatial-temporal resolution of magnetosome biogenesis, we sought to track magnetosomes segregation in pulse-labeled cells by time-lapse. Briefly, cells were pulse-labeled and spotted on agarose pads and the same field of cells was imaged over the course of 7 hours. By this method, an area where no label is detected is presumed to be an area of new

magnetosome synthesis. We observed two major segregation patterns of pulse-labeled magnetosomes (Figure 5). First, pulse-labeled cells that initially exhibited a solid linear localization of Halo-MmsF did not acquire a different localization pattern after 7 hours. Second, a pulse-labeled cell would divide and one daughter cell would receive no pulse-label while the other daughter cell received all of the pulse-label. Time-lapse imaging on agarose pads has two major disadvantages to accurately identifying the sites of magnetosome biogenesis within the chain. First, cells stop dividing and instead begin to lyse after 8 hours of imaging. Second, the position of new magnetosomes has to be inferred by areas that lack pulse-labeling, since it is not possible chase-label and wash the cells on the agarose pad. To circumvent these issues, we attempted to grow the cells in the CellASIC microfluidics plate, which allows for simultaneous imaging and exchange of media on the same population of cells (Figure 6). Preliminary studies show that cells can be grown aerobically in the CellASIC system for 15 hours, and divide three times within this timeframe (Figure 6). Further optimization is required for growth under anaerobic conditions to allow for magnetite biomineralization, as well as for pulse-chase labeling cells in the CellASIC system.

DISCUSSION

In magnetotactic bacteria, the positioning of magnetosomes into a chain across the cell functions to passively align the cell to external magnetic fields (50). This level of subcellular organization must be maintained over many cell generations and each newly made magnetosome must somehow be correctly positioned within the chain. The mechanisms for the correct positioning of new magnetosomes to maintain this subcellular organization remain to be elucidated. Thus far, only two genes, *mamK* and *mamK-like,* have been empirically shown to influence magnetosome chain organization in *Magnetospirillum magneticum* AMB-1 (5, 103). However, despite the presence of misaligned magnetosomes and gaps in the chain, the general plane of alignment is still maintained in the absence of either *mamK* and/or *mamK-like* (5, 103). Furthermore, a magnetosome chain can still form *de novo* in the absence of *mamK*, albeit with a significant number of gaps (5, 101, 102). Thus, we are left with an unsolved puzzle: how are magnetosomes correctly positioned and how is magnetosome organization maintained?

To address this question, our approach was to pulse-label all of the pre-existing magnetosomes and then identify the position of newly-made magnetosomes within the chain by chase-labeling the same cells after several cell generations. By this method, we were able to discern distinct patches of pre-existing versus new magnetosomes, however, no clear pattern of new magnetosome positioning could be identified (Figure 3). The patches of pulse-labeled versus chase-labeled magnetosomes appear to represent distinct magnetosome populations because we confirmed that the pulse-labeled Halo-MmsF protein cannot diffuse between magnetosomes (Figure 2). Furthermore, the pulse-label appears to stably associate with individual magnetosomes because the number of labeled magnetosomes per cell decreases in cell populations that have undergone more cell generations as opposed to an overall decrease in fluorescence with no change in localization (Figure 4).

We attempted to identify the positioning of new magnetosomes by performing time-lapse on pulse labeled cells (Figure 5). If new magnetosome formation occurs stochastically within the chain, we would expect to see the Halo-MmsF localization to change from a solid line to aligned

foci; pulse-labeled cells that initially exhibited a solid linear localization of Halo-MmsF, do not acquire a different localization pattern after 7 hours. One interpretation is that very few new magnetosomes were made within this time frame. It is also possible that the newly made magnetosomes are positioned between pre-existing magnetosomes, however, are undetected due to the resolution limit of light microscopy (~250 nm) (107). Both scenarios can be addressed by extending the time-lapse imaging to visualize more cell divisions, which will presumably increase the number of new, unlabeled magnetosomes that are added to the chain. We also observed several instances where a pulse-labeled cell divided but only one of the daughter cells received the pulse label. This suggests that in some cases, the magnetosome chain is not segregated evenly between daughter cells. Wildtype cells devoid of magnetosomes presumably have all of the machinery to reconstruct a magnetosome chain *de novo*. However, unless magnetosome synthesis is somehow accelerated in the daughter cells, improper magnetosome chain segregation would most likely lead to a sub-population of cells with very few or no magnetosomes. This is inconsistent with previous observations of wildtype AMB-1 imaged by transmission electron microscopy (TEM), which find that the vast majority of cells contain chains of magnetosome crystals (33, 35, 67). Protein stability has not been characterized for Halo-MmsF over such a long time-scale and could potentially account for the lack of fluorescence in certain daughter cells.

These findings are still very preliminary and there are a number of assumptions about the behavior of MmsF that must be addressed through control experiments. First, a major assumption in using Halo-MmsF as a stable magnetosome marker is that Halo-MmsF incorporates into magnetosomes as they are forming and that newly synthesized Halo-MmsF cannot incorporate into pre-existing magnetosomes. Future FRAP experiments using a constitutively expressed GFP-mmsF could potentially answer this question. Since no recovery is observed in Halo-MmsF FRAP experiments, recovery using the GFP-MmsF would indicate that newly synthesized protein is incorporating into pre-existing magnetosomes. Second, we assume that the pulse has labeled the entire pool of pre-existing Halo-MmsF, however, incomplete pulse labeling could result in pre-existing protein getting labeled during the chase. Much like the former assumption, this could result in co-localization of the pulse chase or be responsible for some of the patchy and unpredictable localization observed in the pulse-chase (Figure 3).

Overall, these studies show that Halo-MmsF is an adequate magnetosome marker in that it can be successfully pulse-chase labeled, it does not exhibit noticeable protein dynamics, and it stably associates with magnetosomes over many cell generations. Future studies should be aimed at optimizing the time-lapse imaging conditions for Halo-MmsF and other magnetosome proteins to not only determine how new magnetosomes are positioned within the pre-existing chain, but also, explore magnetosome protein targeting and turnover as they pertain to the different stages of magnetosome formation.

Figures

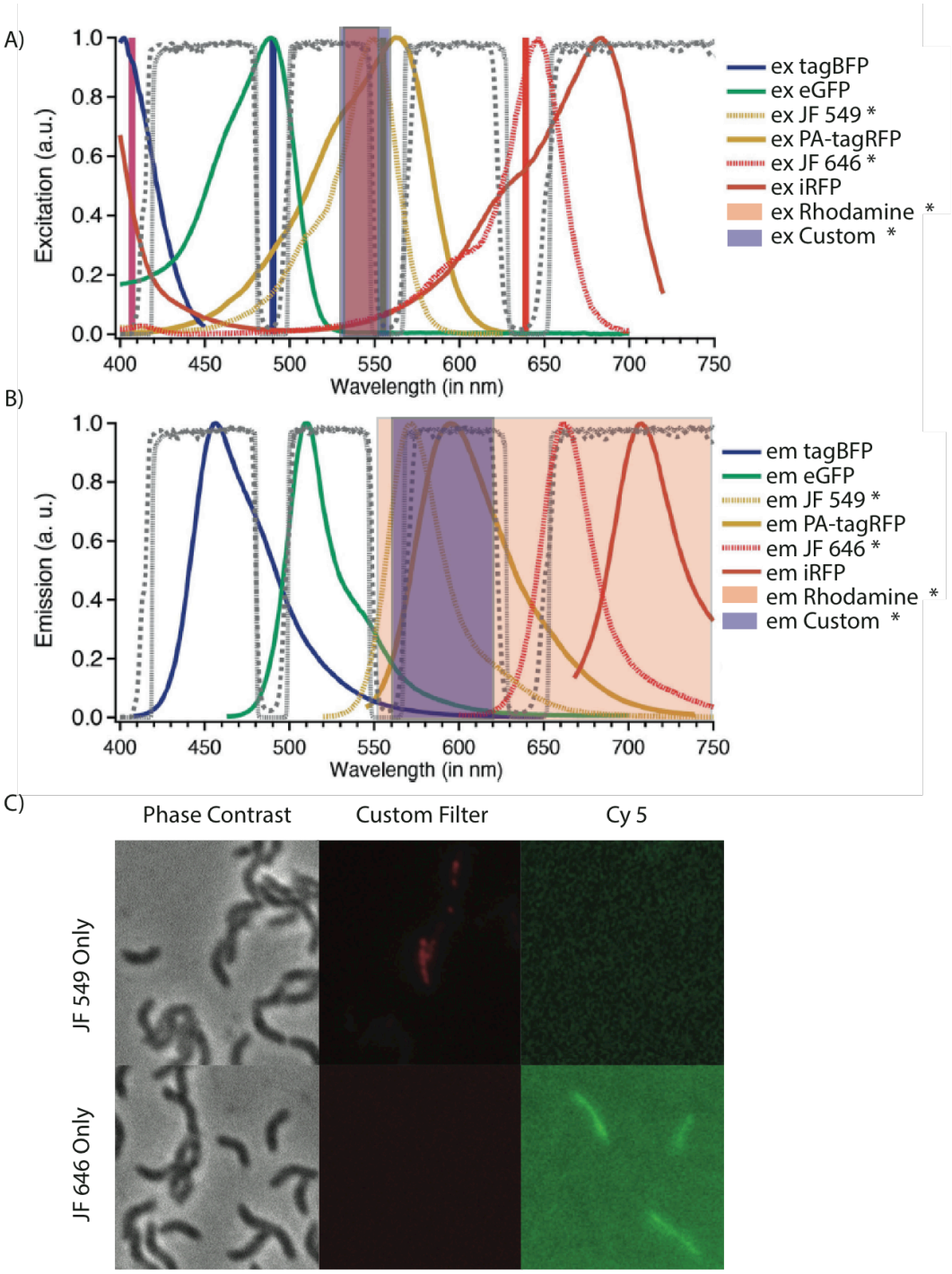

Figure 1. Dual labeling and imaging optimization for JF 549 and JF 646 (A-B) Excitation and emission spectra for JF 549 and JF 646 (asterisks). Excitation and emission windows for standard rhodamine filter (orange, asterisks) versus custom filter (blue, asterisk) are overlayed. Figure adapted from reference (108). (C) Wildtype AMB-1 transformed with pAK983 (halo-mmsF) stained with either JF 549 or JF646. Custom filter cube effectively images JF549 but does not image JF646.

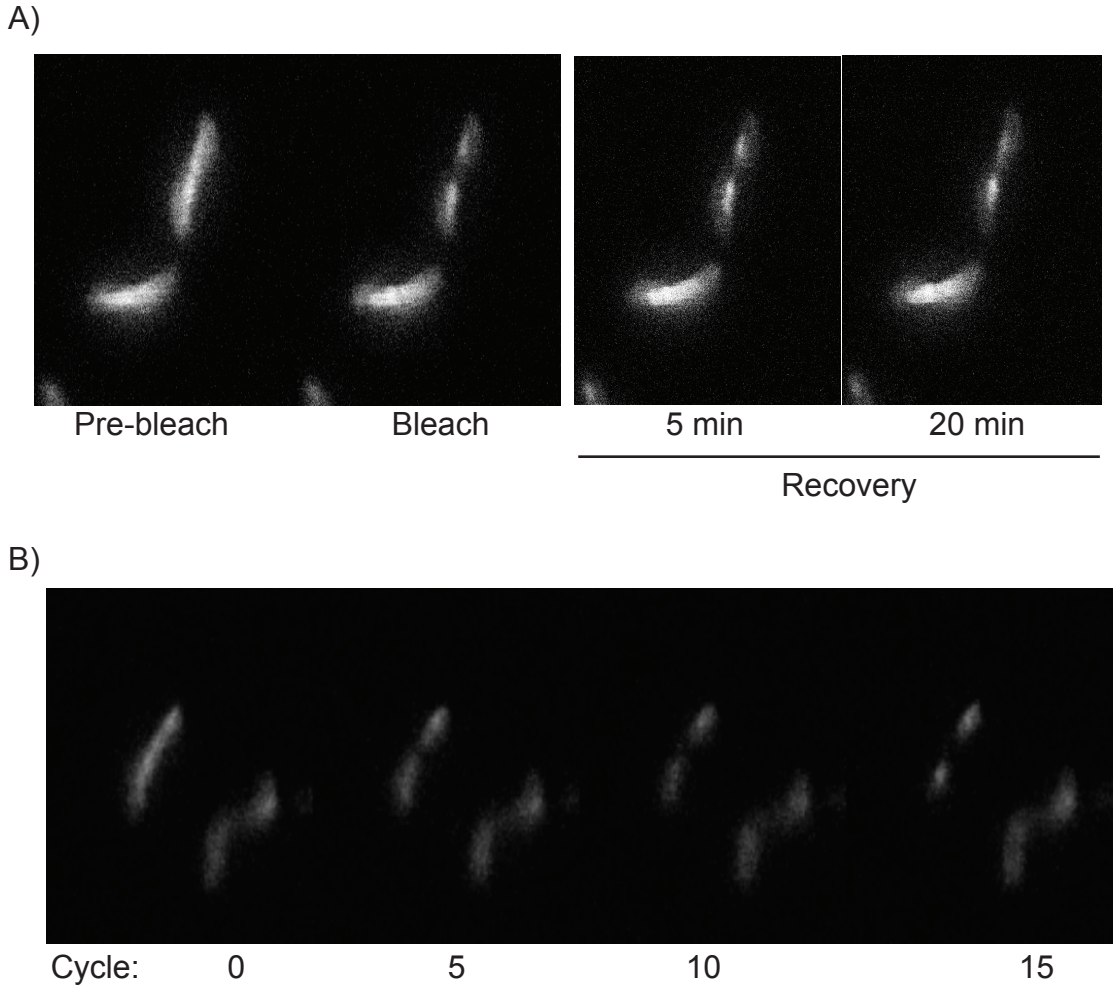

Figure 2. Halo-MmsF does not exhibit protein dynamics in wildtype AMB-1. A) Fluorescence Recovery After Photobleaching (FRAP) of WT/Halo-MmsF stained with JF549. B) Fluorescence Loss in Photobleaching (FLIP) of WT/Halo-MmsF stained with JF549. Cells were exposed to 20 bleach iterations every 10 seconds for 15 cycles. Both FRAP and FLIP experiments were performed by Haley McCausland.

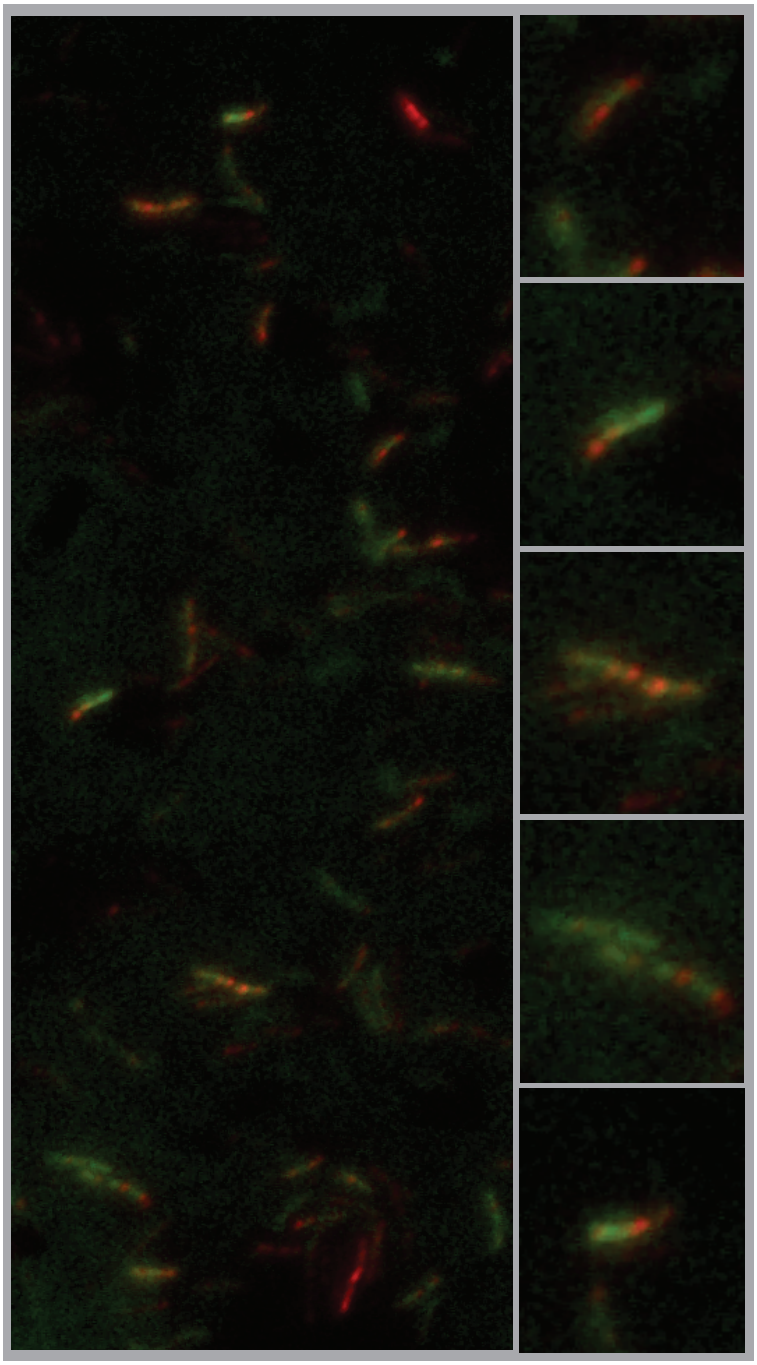

Figure 3. Pulse-chase labeling of Halo-MmsF in wildtype AMB-1. Overlay of JF 549 and JF 646 stain after 24hr pulse chase experiment. Left is a representative field of view. Enlarged images on the right are representative examples of the variations in pulse-chase patterning that are observed.

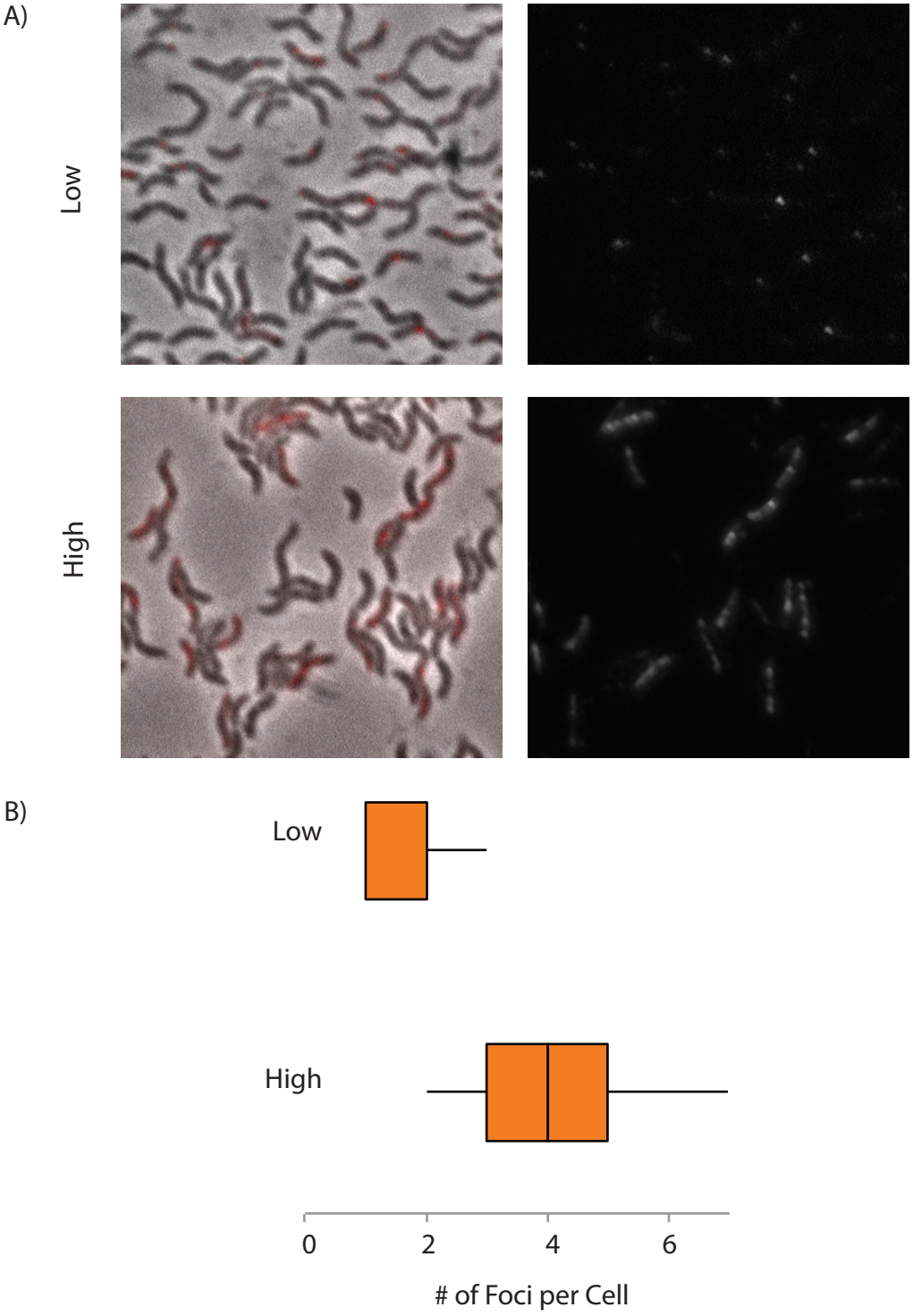

Figure 4. Pulse labeled Halo-MmsF in wildtype AMB-1 and outgrowth. (A) WT/pAK983 cells were stained with JF 549, diluted to either a low (OD400 = 0.01) or high (OD400 = 0.1) cell density and grown overnight to stationary phase. (B) End-point quantification of the number of JF 549 foci per cell that started as either a low or high density cell culture.

A)

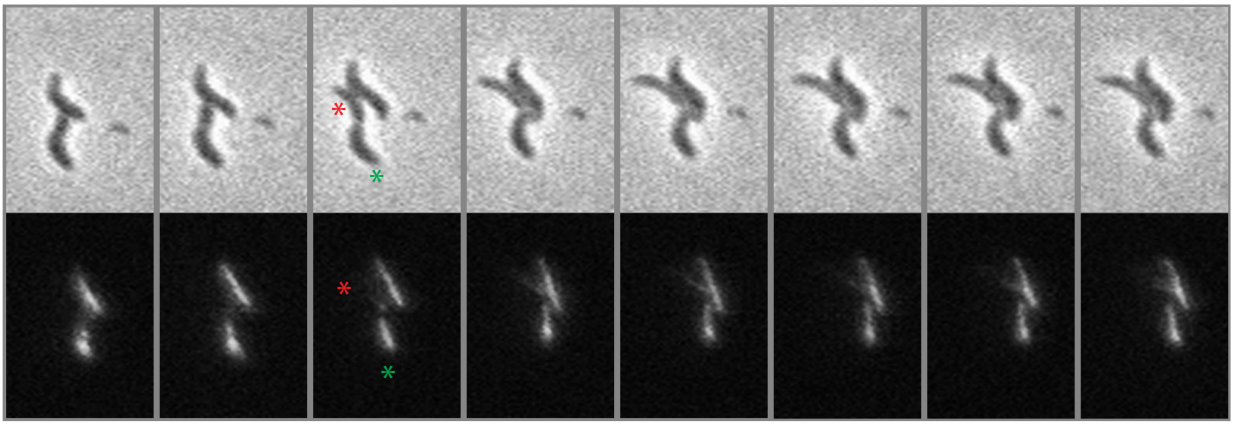

B)

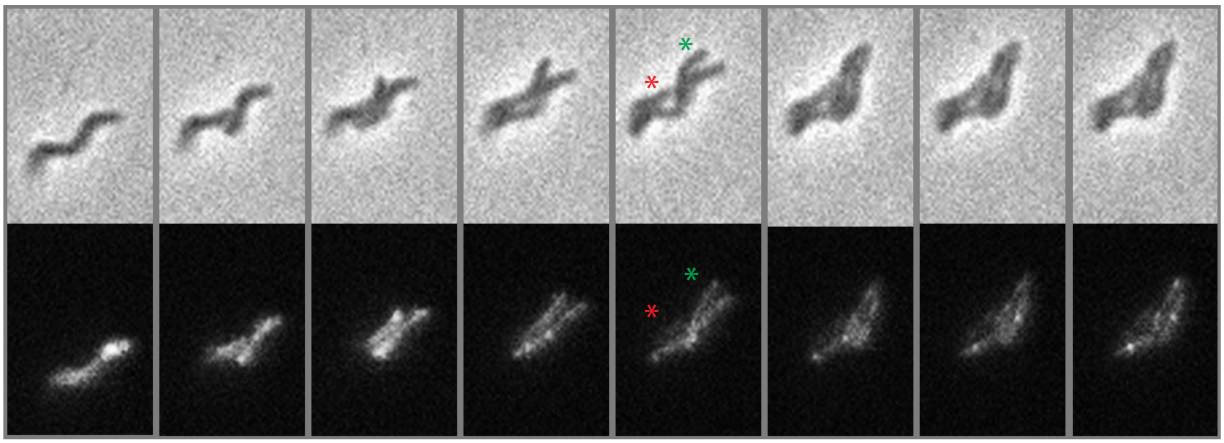

Figure 5. Timelapse of pulse-labeled Halo-MmsF in wildtype AMB-1. Cells were pulse-labelled with JF 549 and spotted on 0.7% agarose pads. Each frame is 1 hour of growth. Astrisks indicate daughter cells that received pulse-label (green) or did not receive pulse label (red).

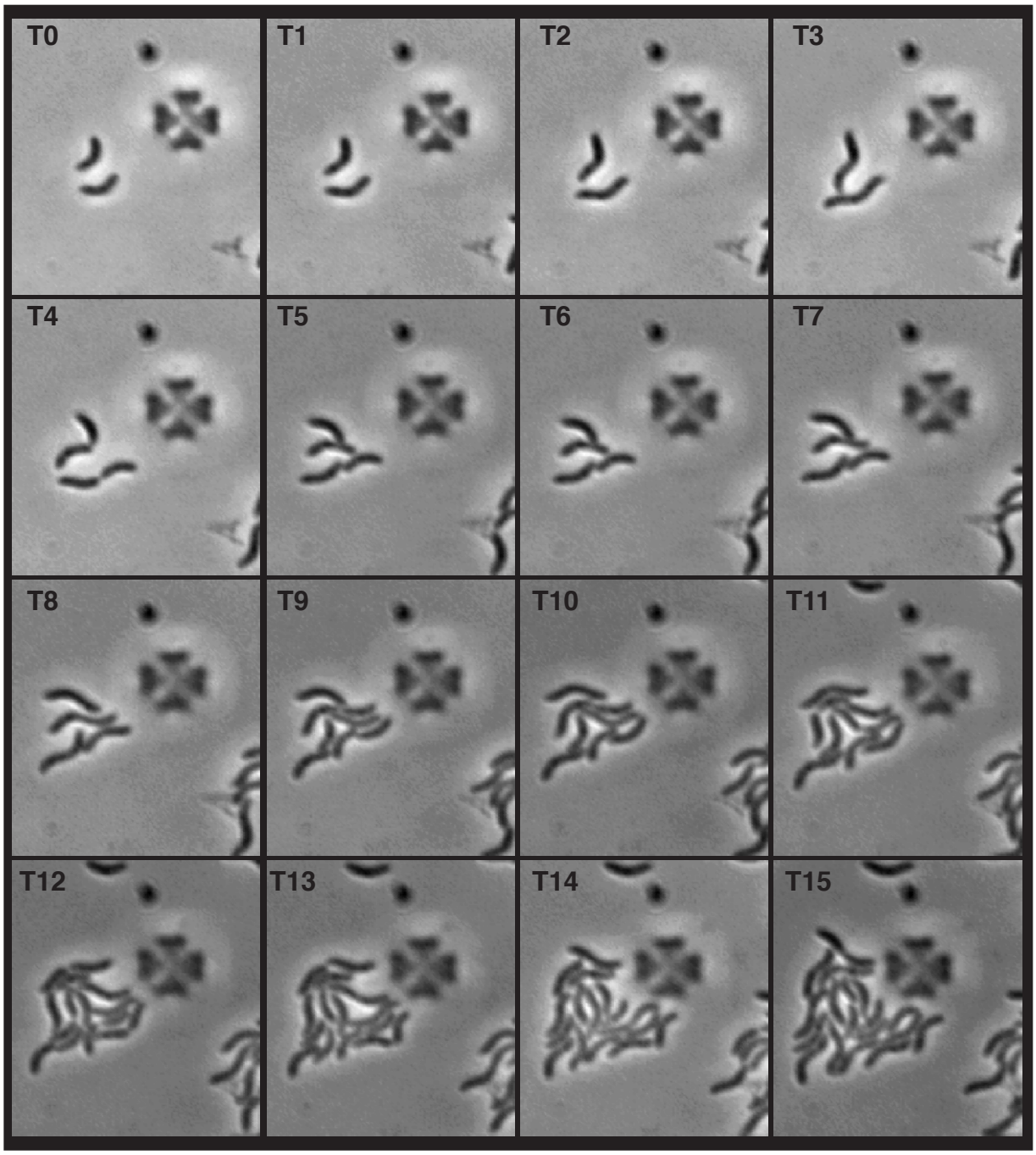

Figure 6. Growth of wildtype AMB-1 in CellASIC™ microfluidic system. Phase contrast images of wildtype AMB-1 over 15 hours of growth in MG medium at 30 degrees Celsius (T = Time in hours). Phase-dark clover structure in all of the frames is a structural pillar in the microfluids plate to ensure an even 0.7 micrometer height.

Plasmid	Description	Plasmid backbone
pAK22	***tac* promoter – *mamK-gfp***	**Reference** (5)
pAK54	***mms16* promoter - *mamQRB***	**pBBR vector**
pAK532	***tac* promoter – *gfp-mmsF***	**Reference** (37)
pAK976	***m-halo* (full length)**	**pAK22**
pAK977	***m-halo* (full length)**	**pAK54**
pAK978	***n-halo* (N-terminal tag)**	**pAK54**
pAK979	***c-halo* (C-terminal tag)**	**pAK54**
pAK983	***halo-mmsF***	**pAK978**

Table 1. Plasmids generated from this work

oAK #	Target	Sequence
EC151	3N-*halo*	actagtgccggaaatctcgagcgtc
EC152	5C-*halo*	gaattcgcagaaatcggtactggctttcc
EC156	5Spe-C*mmsF*	acacaactagtctggccgaggccgcggcg
EC157	3Spe-C*mmsF*	tgtgtactagttcagatccggtgggcgacccagct
EC166	5Eco-*mhalo*	acacagaattcatggcagaaatcggtactggc
EC167	3Spe-*mhalo*	tgtgtactagtctagccggaaatctcgagcg

Table 2. Primers generated from this work

CHAPTER 4

Conclusions and future directions for membrane remodeling and subcellular positioning of magnetosomes

Elias Jose Cornejo-Warner

Department of Plant and Microbial Biology, University of California, Berkeley, CA, USA

ABSTRACT

Although many bacterial organelles have been identified and characterized in terms of their function and morphology, there is still much work to be done to understand the molecular mechanisms control the size, shape and positioning of these subcellular compartments (3, 4). With such a diversity of membrane-bound organelles, it will be interesting to see if the bacteria that make these organelles share common mechanisms for membrane remodeling or if bacteria have devised many ways to achieve subcellular compartmentalization. *Magnetospirillum magneticum* AMB-1 (AMB-1) lends itself as a genetically tractable model system to understand the molecular mechanisms of membrane remodeling and subcellular positioning of at least one bacterial organelle. Prior to this work, a combination of genetic and biochemical studies had culminated into a model that magnetosome formation occurs in the following stages: membrane formation, alignment, and biomineralization and specific genes are required at each stage (33, 34, 61–63). We are now challenged to investigate the how the proteins encoded by these genes function mechanistically and how a chain of magnetosomes is maintained through successive cell divisions.

MAGNETOSOME MEMBRANE REMODELING

Our understanding of magnetosome membrane formation in AMB-1 is currently limited to the mutant phenotypes that are unable to form magnetosomes. The ~18 kilobase *mamAB* region is both required and sufficient for magnetosomes formation (33). Within the *mamAB* region, there are four genes (*mamI, mamL, mamQ, mamB*), which are required for magnetosome formation; however, they are not sufficient to restore magnetosome membrane formation in a strain lacking the *mamAB* region (33). This suggests that other genes within the *mamAB* region participate in membrane remodeling events that remodel the inner membrane to form the magnetosomes. Future studies are needed to identify a minimal gene set that is sufficient to form the magnetosome membrane.

We now know that the magnetosome membrane forms in at least two stages (101). In the first stage, the inner cell membrane is remodeled to create a subcellular compartment. In the second stage, the magnetosome is further remodeled in a manner that appears to coordinate with crystal formation. Thus, the magnetosome membrane is not just a boundary that separates the magnetosome lumen from the cytoplasm (or the periplasm); the size of the compartment dynamically changes to control proper crystal formation. This suggests that perhaps many of the genes that were previously thought to directly control biomineralization, could in fact, act indirectly to control the size and shape of the magnetosome membrane (33). In other words, the “biomineralization” genes that were previously identified in the step-wise model of magnetosome formation could actually be “membrane remodeling” genes. The initial characterization of these mutant phenotypes relied on conventional transmission electron microscopy (TEM) to report on the physical nature of the magnetite crystals, however, future efforts should expand this characterization to include the physical nature of the magnetosome membrane. Using high-

resolution electron cryotomography (ECT) to interrogate the size and shape of the magnetosome membrane in these mutants could reveal how the physical nature of this membrane compartment impact the physical nature of the crystal within. Furthermore, such studies could fill in the gap of knowledge as to which additional genes are involved in remodeling the magnetosome membrane and at which stage of formation.

MAGNETOSOME POSITIONING

By reconstructing the magnetosome chain *de novo*, we showed in this work that magnetosome chain organization relies on two principles: alignment and chain continuity (101). Reconstructing the magnetosome chain in the inducible system revealed that magnetosomes can align at first into a discontinuous chain, then these discontinuities, or gaps, are resolved in a manner that is dependent on *mamK*. A previous body of work has identified and characterized MamK to be bacterial actin-like protein that oligomerizes into dynamic filaments that flank the magnetosome chain in AMB-1 (5, 39, 40). Deleting mamK results in a chain organization defect where the chain becomes discontinuous and many magnetosomes become unaligned from the rest of the magnetosome chain (5). Interestingly, deleting *mamK* or the *mamK* homolog, *mamK-like*, reduces the percentage of cells that can correctly align a magnetosome chain in the population (103). However, *mamK* does not appear to be the only factor needed for magnetosome alignment since in both the *ΔmamK* strain as well as the inducible strain lacking mamK, a magnetosome chain, albeit with a number of gaps, is still able to form (5, 101). Future work is needed to identify additional factors that are responsible for magnetosome alignment. In addition, elucidating the mechanism by which MamK resolves the gaps in the magnetosome chain would be a major breakthrough in our understanding of magnetosome positioning and subcellular organization of membrane-bound organelles in bacteria.

Reconstructing the magnetosome chain *de novo* provided many insights in to the principles that govern magnetosome chain formation and the role of *mamK* (101). However, this scenario does not necessarily represent how wildtype AMB-1 cells deal with organizing magnetosomes and maintaining a magnetosome chain. In wildtype AMB-1, the magnetosome chain is maintained over successive cell divisions by the formation and placement of new magnetosomes to the chain. It is still a mystery as to where new magnetosomes form in relation to the pre-existing magnetosome chain and how they are correctly aligned and positioned. This work established a pulse-chase system that can differentially label pre-existing versus newly formed magnetosome that will hopefully serve future studies to identify the sites of magnetosome biogenesis. The ability to identify the sites of magnetosome biogenesis and visually track magnetosomes throughout their developmental stages is a powerful tool to interrogate the molecular players involved at each of these stages. The Halo tag labeling system that we established in this work will allow us to investigate a larger question of how proteins are targeted to subcellular locations in bacteria and more specifically, how proteins are targeted to organelles.

REFERENCES

1. **Voeltz GK**, **Barr F a**. 2013. Cell organelles. Curr Opin Cell Biol **25**:403–5.
2. **Chan Y-HM**, **Marshall WF**. 2012. How Cells Know the Size of Their Organelles. Science (80-) **337**:1186–1189.
3. **Murat D**, **Byrne M**, **Komeili A**. 2010. Cell biology of prokaryotic organelles. Cold Spring Harb Perspect Biol **2**:a000422.
4. **Cornejo E**, **Abreu N**, **Komeili A**. 2014. Compartmentalization and organelle formation in bacteria. Curr Opin Cell Biol **26C**:132–138.
5. **Komeili A**, **Li Z**, **Newman DK**, **Jensen GJ**. 2006. Magnetosomes are cell membrane invaginations organized by the actin-like protein MamK. Science **311**:242–5.
6. **Spitzer J**, **Poolman B**. 2013. How crowded is the prokaryotic cytoplasm? FEBS Lett **587**:2094–2098.
7. **Kerfeld C a**, **Heinhorst S**, **Cannon GC**. 2010. Bacterial microcompartments. Annu Rev Microbiol **64**:391–408.
8. **Hsin J**, **Chandler DE**, **Gumbart J**, **Harrison CB**, **Sener M**, **Strumpfer J**, **Schulten K**. 2010. Self-assembly of photosynthetic membranes. Chemphyschem **11**:1154–9.
9. **Oostergetel GT**, **van Amerongen H**, **Boekema EJ**. 2010. The chlorosome: a prototype for efficient light harvesting in photosynthesis. Photosynth Res **104**:245–55.
10. **Vothknecht UC**, **Westhoff P**. 2001. Biogenesis and origin of thylakoid membranes. Biochim Biophys Acta **1541**:91–101.
11. **Errington J**. 2003. Regulation of endospore formation in Bacillus subtilis. Nat Rev Microbiol **1**:117–26.
12. **Schlimpert S**, **Klein E a**, **Briegel A**, **Hughes V**, **Kahnt J**, **Bolte K**, **Maier UG**, **Brun Y V**, **Jensen GJ**, **Gitai Z**, **Thanbichler M**. 2012. General protein diffusion barriers create compartments within bacterial cells. Cell **151**:1270–82.
13. **Diekmann Y**, **Pereira-Leal JB**. 2013. Evolution of intracellular compartmentalization. Biochem J **449**:319–31.
14. **Higgins D**, **Dworkin J**. 2012. Recent progress in Bacillus subtilis sporulation. FEMS Microbiol Rev **36**:131–48.
15. **Abanes-De Mello A**, **Sun Y**, **Aung S**, **Pogliano K**. 2002. A cytoskeleton-like role for the bacterial cell wall during engulfment of the Bacillus subtilis forespore 3253–3264.
16. **Broder DH**, **Pogliano K**. 2006. Forespore engulfment mediated by a ratchet-like mechanism. Cell **126**:917–28.
17. **Meyer P**, **Gutierrez J**, **Pogliano K**, **Dworkin J**. 2010. Cell wall synthesis is necessary for membrane dynamics during sporulation of Bacillus subtilis. Mol Microbiol **76**:956–70.
18. **Sharp MD**, **Pogliano K**. 1999. An in vivo membrane fusion assay implicates SpoIIIE in the final stages of engulfment during Bacillus subtilis sporulation. Proc Natl Acad Sci USA **96**:14553–14558.
19. **Sharp MD**, **Pogliano K**. 2003. The Membrane Domain of SpoIIIE Is Required for Membrane Fusion during Bacillus subtilis Sporulation **185**:2005–2008.
20. **Doan T**, **Coleman J**, **Marquis K a**, **Meeske AJ**, **Burton BM**, **Karatekin E**, **Rudner DZ**. 2013. FisB mediates membrane fission during sporulation in Bacillus subtilis. Genes Dev **27**:322–34.
21. **Kawai F**, **Shoda M**, **Harashima R**, **Sadaie Y**, **Hara H**, **Matsumoto K**. 2004. Cardiolipin

Domains in Bacillus subtilis Marburg Membranes **186**:1475–1483.
22. **Matsumoto K**, **Kusaka J**, **Nishibori A**, **Hara H**. 2006. Lipid domains in bacterial membranes. Mol Microbiol **61**:1110–7.
23. **Abecasis AB**, **Serrano M**, **Alves R**, **Quintais L**, **Pereira-Leal JB**, **Henriques AO**. 2013. A genomic signature and the identification of new sporulation genes. J Bacteriol **195**:2101–15.
24. **Ruiz N**, **Kahne D**, **Silhavy TJ**. 2009. Transport of lipopolysaccharide across the cell envelope: the long road of discovery. Nat Rev Microbiol **7**:677–83.
25. **Rigel NW**, **Silhavy TJ**. 2012. Making a beta-barrel: assembly of outer membrane proteins in Gram-negative bacteria. Curr Opin Microbiol **15**:189–93.
26. **Okuda S**, **Freinkman E**, **Kahne D**. 2012. Cytoplasmic ATP hydrolysis powers transport of lipopolysaccharide across the periplasm in E. coli. Science **338**:1214–7.
27. **Tocheva EI**, **Matson EG**, **Morris DM**, **Moussavi F**, **Leadbetter JR**, **Jensen GJ**. 2011. Peptidoglycan remodeling and conversion of an inner membrane into an outer membrane during sporulation. Cell **146**:799–812.
28. **McKenney PT**, **Driks A**, **Eichenberger P**. 2013. The Bacillus subtilis endospore: assembly and functions of the multilayered coat. Nat Rev Microbiol **11**:33–44.
29. **Tocheva EI**, **López-Garrido J**, **Hughes HV**, **Fredlund J**, **Kuru E**, **Vannieuwenhze MS**, **Brun Y V**, **Pogliano K**, **Jensen GJ**. 2013. Peptidoglycan transformations during Bacillus subtilis sporulation. Mol Microbiol **88**:673–86.
30. **Endres RG**. 2012. Intracellular chemical gradients: morphing principle in bacteria. BMC Biophys **5**:18.
31. **Caudron F**, **Barral Y**. 2009. Septins and the lateral compartmentalization of eukaryotic membranes. Dev Cell **16**:493–506.
32. **Komeili A**. 2012. Molecular mechanisms of compartmentalization and biomineralization in magnetotactic bacteria. FEMS Microbiol Rev **36**:232–55.
33. **Murat D**, **Quinlan A**, **Vali H**, **Komeili A**. 2010. Comprehensive genetic dissection of the magnetosome gene island reveals the step-wise assembly of a prokaryotic organelle. Proc Natl Acad Sci USA **107**:5593–8.
34. **Lohße A**, **Ullrich S**, **Katzmann E**, **Borg S**, **Wanner G**, **Richter M**, **Voigt B**, **Schweder T**, **Schüler D**. 2011. Functional analysis of the magnetosome island in Magnetospirillum gryphiswaldense: the mamAB operon is sufficient for magnetite biomineralization. PLoS One **6**:e25561.
35. **Quinlan A**, **Murat D**, **Vali H**, **Komeili A**. 2011. The HtrA/DegP family protease MamE is a bifunctional protein with roles in magnetosome protein localization and magnetite biomineralization. Mol Microbiol **80**:1075–87.
36. **Uebe R**, **Junge K**, **Henn V**, **Poxleitner G**, **Katzmann E**, **Plitzko JM**, **Zarivach R**, **Kasama T**, **Wanner G**, **Pósfai M**, **Böttger L**, **Matzanke B**, **Schüler D**. 2011. The cation diffusion facilitator proteins MamB and MamM of Magnetospirillum gryphiswaldense have distinct and complex functions, and are involved in magnetite biomineralization and magnetosome membrane assembly. Mol Microbiol **82**:818–35.
37. **Murat D**, **Falahati V**, **Bertinetti L**, **Csencsits R**, **Körnig A**, **Downing K**, **Faivre D**, **Komeili A**. 2012. The magnetosome membrane protein, MmsF, is a major regulator of magnetite biomineralization in Magnetospirillum magneticum AMB-1. Mol Microbiol **85**:684–99.
38. **Frankel RB**, **Bazylinski D a**, **Johnson MS**, **Taylor BL**. 1997. Magneto-aerotaxis in

marine coccoid bacteria. Biophys J **73**:994–1000.
39. **Draper O**, **Byrne ME**, **Li Z**, **Keyhani S**, **Barrozo JC**, **Jensen G**, **Komeili A**. 2011. MamK, a bacterial actin, forms dynamic filaments in vivo that are regulated by the acidic proteins MamJ and LimJ. Mol Microbiol **82**:342–54.
40. **Ozyamak E**, **Kollman J**, **Agard D a**, **Komeili A**. 2013. The bacterial actin MamK: in vitro assembly behavior and filament architecture. J Biol Chem **288**:4265–77.
41. **Sonkaria S**, **Fuentes G**, **Verma C**, **Narang R**, **Khare V**, **Fischer A**, **Faivre D**. 2012. Insight into the assembly properties and functional organisation of the magnetotactic bacterial actin-like homolog, MamK. PLoS One **7**:e34189.
42. **Katzmann E**, **Müller FD**, **Lang C**, **Messerer M**, **Winklhofer M**, **Plitzko JM**, **Schüler D**. 2011. Magnetosome chains are recruited to cellular division sites and split by asymmetric septation. Mol Microbiol **82**:1316–29.
43. **Katzmann E**, **Scheffel A**, **Gruska M**, **Plitzko JM**, **Schüler D**. 2010. Loss of the actin-like protein MamK has pleiotropic effects on magnetosome formation and chain assembly in Magnetospirillum gryphiswaldense. Mol Microbiol **77**:208–24.
44. **Philippe N**, **Wu L-F**. 2010. An MCP-like protein interacts with the MamK cytoskeleton and is involved in magnetotaxis in Magnetospirillum magneticum AMB-1. J Mol Biol **400**:309–22.
45. **Sakaguchi S**, **Taoka A**, **Fukumori Y**. 2013. Analysis of Magnetotactic Behavior by Swimming Assay. Biosci Biotechnol Biochem **77**:940–947.
46. **Savage DF**, **Afonso B**, **Chen AH**, **Silver P a**. 2010. Spatially ordered dynamics of the bacterial carbon fixation machinery. Science **327**:1258–61.
47. **Roberts MAJ**, **Wadhams GH**, **Had KA**, **Tickner S**, **Armitage JP**. 2012. ParA-like protein uses nonspeci fi c chromosomal DNA binding to partition protein complexes.
48. **Thompson SR**, **Wadhams GH**, **Armitage JP**. 2006. The positioning of cytoplasmic protein clusters in bacteria. Proc Natl Acad Sci USA **103**:8209–14.
49. **Jain IH**, **Vijayan V**, **Shea EKO**. 2012. Spatial ordering of chromosomes enhances the fi delity of chromosome partitioning in cyanobacteria.
50. **Balkwill DL**, **Maratea D**, **Blakemore RP**. 1980. Ultrastructure of a magnetotactic spirillum. J Bacteriol **141**:1399–408.
51. **Federovitch CM**, **Ron D**, **Hampton RY**. 2005. The dynamic ER: Experimental approaches and current questions. Curr Opin Cell Biol **17**:409–414.
52. **Egner A**, **Jakobs S**, **Hell SW**. 2002. Fast 100-nm resolution three-dimensional microscope reveals structural plasticity of mitochondria in live yeast. Proc Natl Acad Sci USA **99**:3370–3375.
53. **Huotari J**, **Helenius A**. 2011. Endosome maturation. EMBO J **30**:3481–3500.
54. **Tucker JD**, **Siebert CA**, **Escalante M**, **Adams PG**, **Olsen JD**, **Otto C**, **Stokes DL**, **Hunter CN**. 2010. Membrane invagination in Rhodobacter sphaeroides is initiated at curved regions of the cytoplasmic membrane, then forms both budded and fully detached spherical vesicles. Mol Microbiol **76**:833–47.
55. **Niederman R a**. 2013. Membrane development in purple photosynthetic bacteria in response to alterations in light intensity and oxygen tension. Photosynth Res **116**:333–48.
56. **Cameron JC**, **Wilson SC**, **Bernstein SL**, **Kerfeld CA**. 2013. Biogenesis of a Bacterial Organelle: The Carboxysome Assembly Pathway. Cell **155**:1131–1140.
57. **Chen AH**, **Robinson-Mosher A**, **Savage DF**, **Silver P a**, **Polka JK**. 2013. The bacterial carbon-fixing organelle is formed by shell envelopment of preassembled cargo. PLoS One

8:e76127.
58. **Staniland SS**, **Moisescu C**, **Benning LG**. 2010. Cell division in magnetotactic bacteria splits magnetosome chain in half. J Basic Microbiol **50**:392–6.
59. **Schüler D**. 2008. Genetics and cell biology of magnetosome formation in magnetotactic bacteria. FEMS Microbiol Rev **32**:654–672.
60. **Lefèvre CT**, **Bazylinski D a**. 2013. Ecology, diversity, and evolution of magnetotactic bacteria. Microbiol Mol Biol Rev **77**:497–526.
61. **Grünberg K**, **Müller EC**, **Otto A**, **Reszka R**, **Linder D**, **Kube M**, **Reinhardt R**, **Schüler D**. 2004. Biochemical and Proteomic Analysis of the Magnetosome Membrane in Magnetospirillum gryphiswaldense. Appl Environ Microbiol **70**:1040–1050.
62. **Tanaka M**, **Okamura Y**, **Arakaki A**, **Tanaka T**, **Takeyama H**, **Matsunaga T**. 2006. Origin of magnetosome membrane: Proteomic analysis of magnetosome membrane and comparison with cytoplasmic membrane. Proteomics **6**:5234–5247.
63. **Matsunaga T**, **Okamura Y**, **Fukuda Y**, **Wahyudi AT**, **Murase Y**, **Takeyama H**. 2005. Complete genome sequence of the facultative anaerobic magnetotactic bacterium Magnetospirillum sp. strain AMB-1. DNA Res **12**:157–166.
64. **Lefèvre CT**, **Trubitsyn D**, **Abreu F**, **Kolinko S**, **Jogler C**, **de Almeida LGP**, **de Vasconcelos ATR**, **Kube M**, **Reinhardt R**, **Lins U**, **Pignol D**, **Schüler D**, **Bazylinski D a**, **Ginet N**. 2013. Comparative genomic analysis of magnetotactic bacteria from the Deltaproteobacteria provides new insights into magnetite and greigite magnetosome genes required for magnetotaxis. Environ Microbiol **15**:2712–2735.
65. **Rahn-Lee L**, **Byrne ME**, **Zhang M**, **Le Sage D**, **Glenn DR**, **Milbourne T**, **Walsworth RL**, **Vali H**, **Komeili A**. 2015. A Genetic Strategy for Probing the Functional Diversity of Magnetosome Formation. PLoS Genet **11**:e1004811.
66. **Scheffel A**, **Gruska M**, **Faivre D**, **Linaroudis A**, **Plitzko JM**, **Schüler D**. 2006. An acidic protein aligns magnetosomes along a filamentous structure in magnetotactic bacteria. Nature **440**:110–114.
67. **Komeili A**, **Vali H**, **Beveridge TJ**, **Newman DK**. 2004. Magnetosome vesicles are present before magnetite formation, and MamA is required for their activation. Proc Natl Acad Sci USA **101**:3839–44.
68. **Klumpp S**, **Faivre D**. 2012. Interplay of magnetic interactions and active movements in the formation of magnetosome chains. PLoS One **7**:1–11.
69. **Schneider CA**, **Rasband WS**, **Eliceiri KW**. 2012. NIH Image to ImageJ: 25 years of image analysis. Nat Methods.
70. **Kremer JR**, **Mastronarde DN**, **McIntosh JR**. 1996. Computer visualization of three-dimensional image data using IMOD. J Struct Biol **116**:71–6.
71. **Mastronarde D**. 2006. Fiducial marker and hybrid alignment methods for single-and double-axis tomography, p. 163–185. *In* Frank, J (ed.), Electron tomography. Springer, New York.
72. **Iancu C V**, **Tivol WF**, **Schooler JB**, **Dias DP**, **Henderson GP**, **Murphy GE**, **Wright ER**, **Li Z**, **Yu Z**, **Briegel A**, **Gan L**, **He Y**, **Jensen GJ**. 2007. Electron cryotomography sample preparation using the Vitrobot. Nat Protoc **1**:2813–19.
73. **Tivol WF**, **Briegel A**, **Jensen GJ**. 2008. An improved cryogen for plunge freezing. Microsc Microanal **14**:375–379.
74. **Zheng SQ**, **Keszthelyi B**, **Branlund E**, **Lyle JM**, **Braunfeld MB**, **Sedat JW**, **Agard D a**. 2007. UCSF tomography: an integrated software suite for real-time electron microscopic

tomographic data collection, alignment, and reconstruction. J Struct Biol **157**:138–47.
75. **Amat F**, **Moussavi F**, **Comolli LR**, **Elidan G**, **Downing KH**, **Horowitz M**. 2008. Markov random field based automatic image alignment for electron tomography. J Struct Biol **161**:260–275.
76. **Topp S**, **Reynoso CMK**, **Seeliger JC**, **Goldlust IS**, **Desai SK**, **Murat D**, **Shen A**, **Puri AW**, **Komeili A**, **Bertozzi CR**, **Scott JR**, **Gallivan JP**. 2010. Synthetic riboswitches that induce gene expression in diverse bacterial species. Appl Environ Microbiol **76**:7881–7884.
77. **Gibson DG**, **Young L**, **Chuang R**, **Venter JC**, **Hutchison CA**, **Smith HO**. 2009. Enzymatic assembly of DNA molecules up to several hundred kilobases. Nat Methods **6**:343–345.
78. **Sadler JR**, **Sasmor H**, **Betz JL**. 1983. A perfectly symmetric lac operator binds the lac repressor very tightly. Proc Natl Acad Sci USA **80**:6785–6789.
79. **Nudelman H**, **Zarivach R**. 2014. Structure prediction of magnetosome-associated proteins. Front Microbiol **5**:9.
80. **Jensen GJ**, **Briegel A**. 2007. How electron cryotomography is opening a new window onto prokaryotic ultrastructure. Curr Opin Struct Biol **17**:260–7.
81. **Li Z**, **Jensen GJ**. 2009. Electron cryotomography: a new view into microbial ultrastructure. Curr Opin Microbiol **12**:333–40.
82. **Rudner DZ**, **Losick R**. 2010. Protein Subcellular Localization in Bacteria. Cold Spring Harb Perspect Biol **2**:a000307–a000307.
83. **Ding Y**, **Li J**, **Liu J**, **Yang J**, **Jiang W**, **Tian J**, **Li Y**, **Pan Y**, **Li J**. 2010. Deletion of the ftsZ-like gene results in the production of superparamagnetic magnetite magnetosomes in Magnetospirillum gryphiswaldense. J Bacteriol **192**:1097–1105.
84. **Müller FD**, **Raschdorf O**, **Nudelman H**, **Messerer M**, **Katzmann E**, **Plitzko JM**, **Zarivach R**, **Schüler D**. 2014. The FtsZ-like protein FtsZm of Magnetospirillum gryphiswaldense likely interacts with its generic homolog and is required for biomineralization under nitrate deprivation. J Bacteriol **196**:650–659.
85. **Rioux JB**, **Philippe N**, **Pereira S**, **Pignol D**, **Wu LF**, **Ginet N**. 2010. A second actin-like mamk protein in magnetospirillum magneticum AMB-1 encoded outside the genomic magnetosome island. PLoS One **5**:e9151.
86. **Mann HB**, **Whitney DR**. 1947. On a Test of Whether one of Two Random Variables is Stochastically Larger than the Other. Ann Math Stat **18**:50–60.
87. **Yamamoto a**, **DeWald DB**, **Boronenkov I V**, **Anderson R a**, **Emr SD**, **Koshland D**. 1995. Novel PI(4)P 5-kinase homologue, Fab1p, essential for normal vacuole function and morphology in yeast. Mol Biol Cell **6**:525–539.
88. **McMahon HT**, **Gallop JL**. 2005. Membrane curvature and mechanisms of dynamic cell membrane remodelling. Nature **438**:590–6.
89. **Mim C**, **Unger VM**. 2012. Membrane curvature and its generation by BAR proteins. Trends Biochem Sci **37**:526–33.
90. **Stachowiak JC**, **Hayden CC**, **Sasaki DY**. 2010. Steric confinement of proteins on lipid membranes can drive curvature and tubulation. Proc Natl Acad Sci USA **107**:7781–6.
91. **McMahon HT**, **Boucrot E**. 2011. Molecular mechanism and physiological functions of clathrin-mediated endocytosis. Nat Rev Mol Cell Biol **12**:517–533.
92. **Shibata Y**, **Shemesh T**, **Prinz W a.**, **Palazzo AF**, **Kozlov MM**, **Rapoport T a.** 2010. Mechanisms determining the morphology of the peripheral ER. Cell **143**:774–788.

93. **Rafelski SM**. 2013. Mitochondrial network morphology: building an integrative, geometrical view. BMC Biol **11**:71.
94. **Baumgart T**, **Capraro BR**, **Zhu C**, **Das SL**. 2011. Thermodynamics and mechanics of membrane curvature generation and sensing by proteins and lipids. Annu Rev Phys Chem **62**:483–506.
95. **Tanaka M**, **Arakaki A**, **Matsunaga T**. 2010. Identification and functional characterization of liposome tubulation protein from magnetotactic bacteria. Mol Microbiol **76**:480–8.
96. **Govindarajan S**, **Nevo-Dinur K**, **Amster-Choder O**. 2012. Compartmentalization And Spatio-Temporal Organization Of Macromolecules In Bacteria. FEMS Microbiol Rev **36**:1005–1022.
97. **Butler RF**, **Banerjee SK**. 1975. Theoretical single-domain grain size range in magnetite and titanomagnetite. J Geophys Res **80**:4049.
98. **Matsunaga T**, **Sakaguchi T**, **Tadokoro F**. 1991. Microbiology Biotedmoto Magnetite formation by a magnetic bacterium capable of growing aerobically **35**:651–655.
99. **Gorby YA**, **Beveridge TJ**, **Blakemore RP**. 1988. Characterization of the Bacterial Magnetosome Membrane **170**:834–841.
100. **Frankel RB**, **Dennis W**. Magneto-Aerotaxis.
101. **Cornejo E**, **Subramanian P**, **Li Z**, **Jensen GJ**. 2016. Dynamic Remodeling of the Magnetosome Membrane Is Triggered by the Initiation of Biomineralization **7**:1–9.
102. **Raschdorf O**, **Forstner Y**, **Kolinko I**, **Uebe R**, **Plitzko JM**. 2016. Genetic and Ultrastructural Analysis Reveals the Key Players and Initial Steps of Bacterial Magnetosome Membrane Biogenesis 1–23.
103. **Abreu N**, **Mannoubi S**, **Ozyamak E**, **Pignol D**, **Ginet N**, **Komeili A**. 2014. Interplay between two bacterial actin homologs, MamK and MamK like, is required for the alignment of magnetosome organelles in Magnetospirillum magneticum AMB-1. J Bacteriol **196**:3111–3121.
104. **Manual T**. HaloTag ® Technology : Focus on Imaging HaloTag ® Technology : Focus on Imaging.
105. **Grimm JB**, **English BP**, **Chen J**, **Slaughter JP**, **Zhang Z**, **Revyakin A**, **Patel R**, **Macklin JJ**, **Normanno D**, **Singer RH**, **Lionnet T**, **Lavis LD**. 2015. A general method to improve fluorophores for live-cell and single-molecule microscopy. Nat Methods **12**:4–7.
106. **Nenninger A**, **Mastroianni G**, **Robson A**, **Lenn T**, **Xue Q**, **Leake MC**, **Mullineaux CW**. 2014. Independent mobility of proteins and lipids in the plasma membrane of Escherichia coli. Mol Microbiol **92**:1142–53.
107. **Galbraith CG**, **Galbraith J a**. 2011. Super-resolution microscopy at a glance. J Cell Sci **124**:1607–11.
108. **English BP**, **Singer RH**. 2015. A three-camera imaging microscope for high-speed single- molecule tracking and super-resolution imaging in living cells. Proc SPIE Int Soc Opt Eng **9550**:1–11.